Cement and Concrete Composites 114 (2020) 103821

Contents lists available at ScienceDirect

Cement and Concrete Composites

journal homepage: http://www.elsevier.com/locate/cemconcomp

# In-situ assessment of the water-penetration resistance of polymer modified cement mortars by μ-XCT, SEM and EDS

Yu Peng [a], Guorong Zhao [b], Yuxuan Qi [a], Qiang Zeng [a,*]

[a] College of Civil Engineering and Architecture, Zhejiang University, Hangzhou, 310058, China
[b] School of Materials Science and Engineering, Tongji University, Shanghai, 201804, China

ARTICLE INFO

*Keywords:*
Anti-penetration
Polymers
X-ray computed tomography
Microstructure

ABSTRACT

Anti-water-penetration techniques are important to raise the durability of cement-based materials (CBMs). Here the water penetration resistances of cement mortars with ethylene-vinyl acetate copolymer (EVA) and styrene butadiene rubber (SBR) were in-situ and non-destructively probed by micro-focus X-ray computed tomography (μ-XCT). Caesium Chloride (CsCl) was mixed in water to enhance the contrast gradients of μ-XCT images. SEM and EDS tests were provided to assess the mortar microstructure changes induced by water penetration. Results show that the CsCl enhancement helps trace the water penetration fronts, while exerting minor influences on the water penetration kinetics. The polymers can greatly raise the resistance against the water penetration into the cement mortars. The pore blocking induced by the formation of polymer films on the surfaces of cement grains and aggregates may account for the enhanced water-penetration resistance. The findings of this work provide a new method to track the water penetration in CBMs by μ-XCT and deepen the knowledge in the anti-water mechanisms of polymer-modified cement materials.

## 1. Introduction

Materials based on ordinary Portland cement (OPC) (or cement-based materials, CBMs) have been massively used in constructions and infrastructures since the invention of OPC in the eighteenth century [1]. Though OPC concrete shows many advantages (e.g., low costs, high compressive strengths, wide resources and versatilities in fabrication and casting), its durability problems attract increasingly raised attentions nowadays because most of concrete constructions are facing or will face performance deteriorations [2]. Many factors, including material components, curing schemes and temperature, hazard species, harsh environments, and external loads, can affect concrete durability [3–7]. Most durability problems or performance degradations, somehow, show connections to the migration of harmful species, like chloride ions, into concrete material matrix, which leads to complex physico-chemical processes, such as the phase transformation, decomposition of minerals and microstructure degradation [8,9]. In CBMs, water is not only an indispensable reactant for cement hydration, but also an essential carrier of various aggressive agents. Indeed, water participates in almost all processes of decomposition and deterioration in CBMs [10]. Therefore, the understanding of the water permeating capacities and routes is vitally important to assess the durability of CBMs [11–13].

Normally, water penetration in and through a porous material mainly relies on the pore network, which can be characterized by several pore parameters, e.g., total open porosity, pore size distribution and pore connectivity [14–16]. The improvement of the pore characteristics has been recognized as an effective way to enhance the water-penetration resistance of CBMs. Following this regime, thin inorganic particles are generally incorporated into cementitious system to refine the pore structure of CBMs. Micro inorganic particles (e.g., silica fume, fly ash, ground slag and micro limestone powder) can physically act as the micro fillers to fill the inter-particle spaces and/or chemically react with the hydration products to eliminate the pores. These actions would make the microstructure of CBMs denser, and as a consequence, the water permeability can be depressed [17–24].

Recently, organic additives play the continually raised roles in tuning the performance of CBMs. Polymers, in the form of either latex or redispersible powder, when added into cement paste, show promising potentials in the controls of flexural strength, flexibility and adhesion, as well as the resistance against water penetration [25–28]. For example, acrylic polymers modified cementitious coatings can reduce the water content of concrete under wet conditions, as well as slow down the

* Corresponding author.
*E-mail address:* cengq14@zju.edu.cn (Q. Zeng).

https://doi.org/10.1016/j.cemconcomp.2020.103821
Received 20 May 2020; Received in revised form 11 September 2020; Accepted 16 September 2020
Available online 19 September 2020

chloride penetration in concrete [29]. Cellulose ether can decrease the water permeability by plugging part of the cement porosity [30].

Ethylene-vinyl acetate copolymer (EVA) and styrene butadiene rubber (SBR) may be two of the most widely used polymers to tune the microstructure and durability performance of CBMs. Experimental studies testified that SBR and EVA can not only improve the CBMs' workability, but also improve the resistance against chloride diffusion and water absorption by refining pore structure [31,32]. It was reported that a 15% addition of SBR or EVA in CBMs can substantially decrease the chloride penetration rate under harsh cyclic wetting-drying loads [33]. The incorporation of SBR into calcium aluminate cement can also reduce the open porosity and drastically lower the water absorption, suggesting the high compatibility between polymers and different binders [34]. These performance modifications rely mostly on the formation of polymer film networks and the interactions between the film and cement particles (and other particles) [35–37]. Our recent work suggested that EVA and SBR, by forming polymer films on the un-reacted cement particles and hydration products, can dramatically retard the cement hydration through depressing the dissolution of the silicate and aluminate minerals, resulting in the increases of Ca/Si ratios in the products layer and the decrease of the CH content [38].

While documents on the anti-penetration of polymer-modified cement materials (PMCMs) are expanding, the underlined mechanisms, however, remain far from being fully understood. A vital challenge comes from the lack of the techniques that can in-situ probe the water penetration/permeation paths and fronts in CBMs. Conventional tests, e.g., the pressurized water penetration test [39–41] and the mass gain (or height rise) test [42,43], only provide some macro quantities to assess the transport properties of CBMs in statistical manners. For better understanding the water penetration/permeation in CBMs with spatial information, tomographic techniques have been developed, such as, electric tomography [44,45], γ-ray radiography [46,47], neutron radiography [48,49], low flied nuclear magnetic resonance (LF-NMR) [50,51] and nano-or micro-focused X-ray computed tomography (Nano-XCT/μ-XCT) [52,53]. Among these testing techniques, the neutron radiography can provide the high contrast images of concrete with water migration because neutron signals are sensitive to hydrogen. However, the light sources of neutrons are not available in most concrete research laboratories. LF-NMR measurement is sensitive to water but may be hard to detect the solid phases in CBMs.

μ-XCT has attracted the increasingly raised attention in the field of concrete science and engineering because of its non-destructiveness, ease of use, and non-pretreatment of samples. With those features, μ-XCT has been widely used to characterize the microstructure of CBMs with/without environmental actions [54–58]. For instance, μ-XCT was applied to evaluate the pore tortuosity of CBMs [59,60], an important pore parameter affecting the permeability and permeation paths of fluids in CBMs [61,62]. However, the direct uses of μ-XCT to investigate the water (and other liquids) penetration in CBMs are shapely limited because pure water has little impact on X-ray attenuation when X-ray beams penetrate through a water filled porous specimen. To enhance the signals of X-ray attenuation provided by the water penetration, complex algorithms may be required to separate the water-filled phase in μ-XCT images [63].

An alternative way to overcome the difficulties in the acquisition of highly contrast μ-XCT images is to use some agents with high X-ray attenuations, e.g., Caesium (Cs), Iodine (I), Bromine (Br) and Mercury (Hg) [53,64]). Caesium Chloride (CsCl) may be a preferable agent for tracing the water penetration in porous materials, because it has high X-ray attenuation and is soluble to water and other liquids (e.g., ethanol and methanol) [65].

Inspired by these evidences, here we used a μ-XCT technique with the X-ray attenuation enhancements by a CsCl solution to track the water penetration fronts in cement mortars modified by EVA and SBR. Ponding tests were performed on the PMCMs for the penetration of the CsCl solution. Scanning electron microscopy (SEM) and energy-dispersive X-ray spectroscopy (EDS) tests were conducted to measure the microstructure and element alterations caused by the invasion of the CsCl solution. Profound discussions were presented to explore the interactions between the polymers and the cement grains/aggregates and their impacts on the water penetrations. The obtained results help explore the anti-water penetration mechanisms of PMCMs.

## 2. Materials and methods

### 2.1. Materials and preparation of specimens

A Chinese P·II Portland cement (PII 52.5) was used as the only binder, and its physical properties, chemical composition and main minerals are listed in Table 1. Quartz sands conforming to the Chinese standard GSB 08-1337-2018 were used as the aggregate.

Two kinds of re-dispersible polymer powders, ethylene-vinyl acetate copolymer (EVA) and styrene butadiene rubber (SBR), were used to prepare the PMCM specimens. The physico-chemical properties of the EVA and SBR are listed in Table 2. The polymers show the similar values of glass temperature and contents of solid and ash, but the different values of particle size, density and lowest film-formation temperature.

Practically, the production of re-dispersible polymer powders consists of: (1) the preparation of the parent polymer emulsion, and (2) the spray drying of the emulsion. To prevent the polymer particles from coalescence during the spray drying, hydrophilic protective colloids and anti-caking agents are added to the emulsions. Here a polyvinyl alcohol was adopted as the colloidal stabilizer for both polymers; and micro calcium carbonate and kaolin were used as the anti-caking agent of SBR and EVA, respectively. Fig. 1 shows the micro morphology of raw polymer powders and the element distributions of local polymer particles and anti-caking agent determined by EDS. Backscattered electron (BSE) image mode was used to identify different phases (Fig. 1A and B). The gray ball-like particles are polymer particles and the white grains are micro calcium carbonate or kaolin particles (see the EDS results in Fig. 1C).

Mortar specimens were prepared with a constant water-to-cement (w/c, wt%) ratio of 0.5, sand-to-cement (s/c, wt%) ratio of 3.0 and polymer-to-cement (p/c, wt%) ratio of 0.1. After a normal mixing process, the fresh mortar slurries were casted into steel moulds with the dimensions of $40 \times 40 \times 160$ mm$^3$. Mortar prisms with a primary curing for 24 h were demoulded and removed into a chamber in temperature of $20 \pm 2$ °C and relative humidity of 90% for further curing to 28 d.

### 2.2. Formation of polymer film

The film formation process of the pure polymer emulsions on glass surfaces was investigated, because this process would be a main factor that influences the performance of PMCMs. This test also helps understand the formation of polymer films in mortar matrix and their impacts on mortar microstructure. The experiment procedures and main results are shown in Fig. 2. First, the polymer powders were mixed with distilled

**Table 1**
Chemical compositions and physical properties of the cement.

| Physical properties of cement | | Chemical compositions of cement/% | | Mineral compositions of clinker/% | |
|---|---|---|---|---|---|
| Fineness 80/% | 1.7 | $SiO_2$ | 21.89 | $C_3S$ | 57.34 |
| Specific surface area m$^2$/kg | 346 | $Al_2O_3$ | 4.18 | $C_2S$ | 18.90 |
| Standard consistency/% | 24 | $Fe_2O_3$ | 3.45 | $C_4AF$ | 11.25 |
| Soundness/mm | 0.5 | CaO | 62.03 | $C_3A$ | 6.47 |
| Initial setting time/min | 169 | MgO | 2.57 | Others | 6.04 |
| Final setting time/min | 253 | $SO_3$ | 2.93 | | |
| Flexural strength (3d)/MPa | 4.0 | f-CaO | 0.93 | | |
| Compressive strength (3d)/MPa | 25.1 | $Na_2O_{eq}$ | 0.57 | | |
| Loss on ignition/(%) | 1.71 | $Cl^-$ | 0.01 | | |
| | | Others | 1.44 | | |

**Table 2**
Physico-chemical properties of the EVA and SBR.

| Polymer | Solid content/ % | Ash content at 600 °C/% | Average particle size/ μm | Density/g. $cm^{-3}$ | Lowest film formation temperature/°C | Glass temperature/ °C | Protective colloid |
|---|---|---|---|---|---|---|---|
| EVA | 99 ± 1 | 11 ± 2 | 3.10 | 1.3 | 4 | 15 | polyvinyl alcohol |
| SBR | 99 ± 1 | 12 ± 2 | 2.46 | 0.91 | 8 | 15 | polyvinyl alcohol |

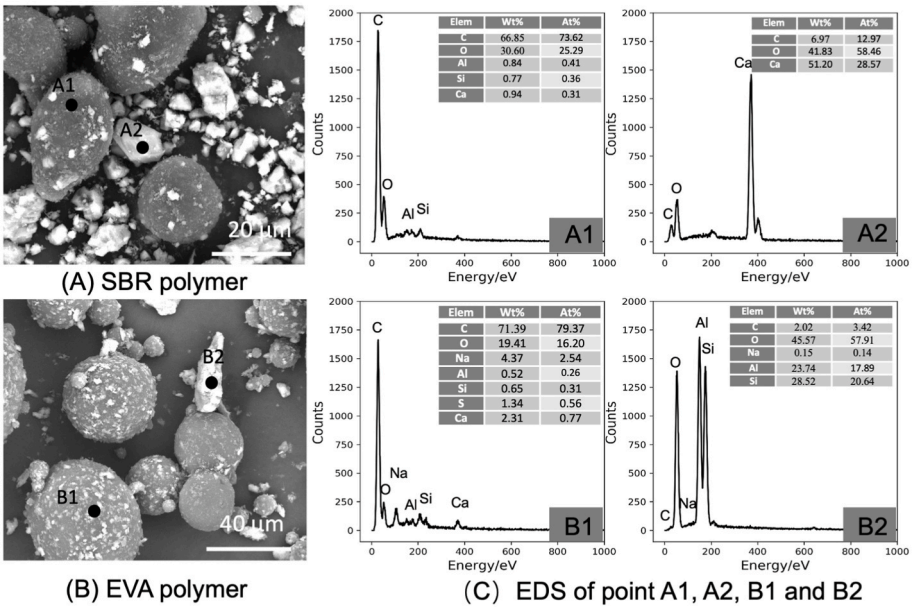


**Fig. 1.** Micro morphology of SBR (A) and EVA (B) as received: BSE images showing the different gray levels between the polymer particles and anti-caking agents (left panels); (C) EDS data at different positions showing different element distributions (middle and right panels).

water to prepare the homogeneously distributed polymer suspensions. The prepared suspensions are like opaque milk (Fig. 2A). Then a drop of each suspension was dripped on a glass slide and exposed to the air at room temperature. After the water was evaporated, the dried polymer emulsions were achieved (Fig. 2B). SEM tests were performed on the dried polymer emulsions. High-magnification SEM images show the polymer films formed by the coalescence of the polymer particles with the sizes of 150–200 nm for SBR (Figs. 2C) and 800–1000 nm for EVA (Fig. 2D), respectively.

### 2.3. Specimens for strength and ponding tests

At the curing ages of 1, 3, 7 and 28 d, the compressive and flexural tests of the mortars were conducted according to Chinese standard GB/T 17671-2005. Three data of each material were averaged to obtain the reliable strength.

The mortar cubes with the dimensions of 20 × 20 × 20 $mm^3$ (Fig. 3A) were cut by an Abrasi-Met 250 manual cutter for ponding tests. The cubes were oven-dried for 48 h at 40 °C to reduce the microstructure alterations induced by drying. The pre-dried mortar cubes were then coated with an epoxy resin to control the water penetration direction. Specifically, five faces of each cubic specimen were sealed by the epoxy resin, and only one face was open for water migration (Fig. 3B). After the hardening of the surface epoxy resin, the reference (Ref.), SBR and EVA mortar cubes were immersed in a CsCl solution (30 wt%) for the ponding tests. During the tests, the un-sealed surface of each specimen was always kept upward, so the CsCl solution could invade the open space of the mortars from top to bottom. The immersion depth (distance to the water surface) was 10 mm (Fig. 3C).

### 2.4. Mass gain

To determine if the presence of CsCl in water affects the penetration dynamics of cement mortars, two sets of cubic mortar specimens were prepared and immersed in pure water and in the CsCl solution for mass gain tests in parallel. The mass gain of each cubic mortar during the ponding test was quantitatively measured by a balance (with the accuracy of 0.1%). The mass gain of water ($\Delta w$) was calculated by comparing the current mass ($w_t$) to the pre-dried one ($w_0$) as follows:

$$\Delta w = \frac{w_t - w_0}{w_0} \times 100\% \quad (1)$$

Generally, the depth ($\Delta L$) or mass ($\Delta w$) of spontaneous absorption in porous materials is governed by the Lucas-Washburn (LW) equation [66]:

$$\Delta L = S_l\sqrt{t} \text{ or } \Delta w = S_m\sqrt{t} \quad (2)$$

where $S_l$ (m/$s^{0.5}$) and$S_m$ (g/$s^{0.5}$) are the depth sorptivity and mass sorptivity, respectively, which both characterize the liquid penetration rates.

If a material has a homogenously distributed pore structure, the mass sorptivity can be uniquely related to the depth sorptivity by $S_m = \rho_l A \varnothing S_l$, where $\rho_l$ is the liquid density (g/$m^3$), $A$ is the sorption area ($m^2$), $\Phi$ is the porosity of the specimen (%). Both the mass and depth sorptivities of a porous material are associated with the material pore structure and the physical properties of the sorption liquid. So, the intrinsic sorptivity were introduced to avoid the influences of the liquid properties, which is given by Ref. [66]:

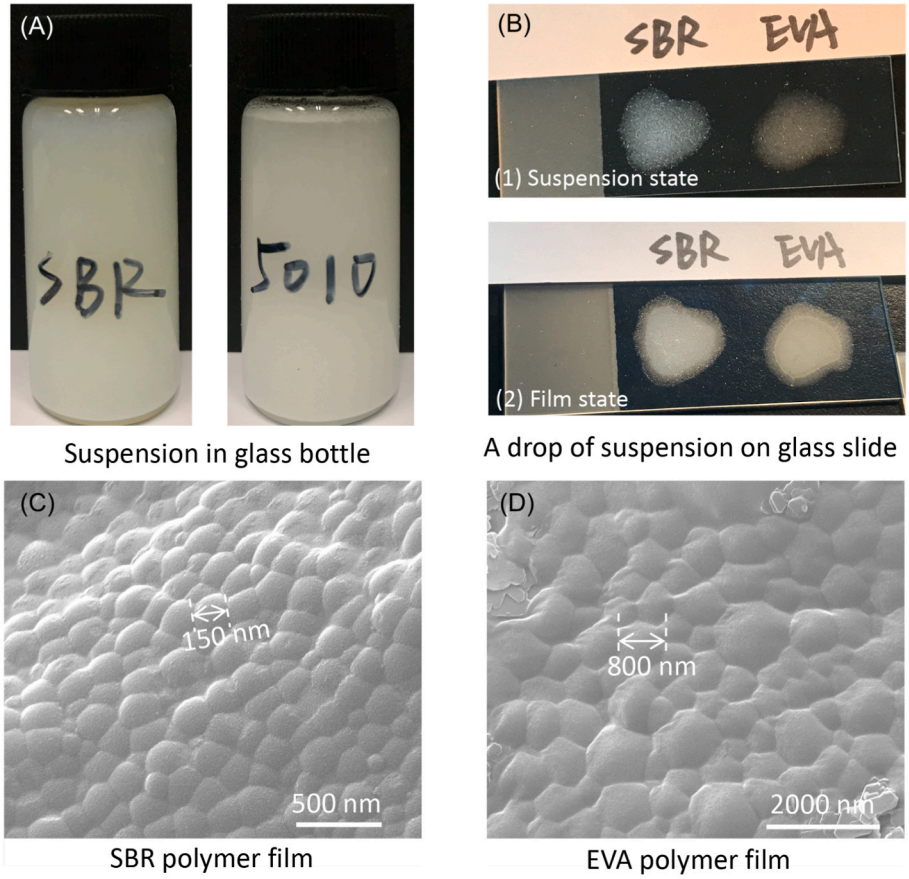


**Fig. 2.** (A) Preparation of polymer emulsion suspensions; (B) drops of SBR and EVA suspensions on a glass slide (1) and the formed films after drying (2); SEM images of (C) SBR and (D) EVA films.

$$S_i = \frac{S_l}{\sqrt{\gamma/\mu}} = \frac{S_m}{\rho_l A \varnothing \sqrt{\gamma/\mu}} \tag{3}$$

where $\gamma$ and $\mu$ are the surface tension (N/m) and dynamic viscosity (Pa·s) of the liquid.

### 2.5. X-ray computed tomography

μ-XCT scans were conducted on each mortar cube before immersion and at the immersion time of 10, 20, 40,70, 190 and 310 min immediately after the mass measurement. The device of XTH255/320 LC (Nikon, Japan) equipped with a high-resolution detector (2000 × 2000 pixels) was used to acquire the X-ray transmission projections at the accelerating voltage of 120 kV and the beam current of 80 μA. Before each μ-XCT test, a cubic mortar specimen was attached on the sample holder frame with the distances to the X-ray sources of 70.4 mm and to the detector of 940.4 mm (Fig. 3D). A Cu filter with the thickness of 0.25 mm was applied between the X-ray source and the sample.

When μ-XCT test began, the cubic mortar specimen rotated evenly by 360°, and X-ray beams penetrated through the specimen and the attenuated X-ray signals were recorded by the detector at different positions and time (Fig. 3D). The X-ray transmission projections at different angles can be used to for 3D microstructure computation (Fig. 3E). In this work, the exposing time for each projection was 0.5 s, and totally, 2500 projections were generated for completing the scans of a sample.

The huge raw projections dataset of each sample (18.6 GB) was then loaded into the CTPro software based on back-projection algorithms to generate numerous gray images before further analysis (Fig. 3F). The beam hardening, noise as well as ring artifacts were manually controlled. The massive image sets were then loaded in the software of VG Studio MAX 3.1 for microstructure analysis (Fig. 3G). The voxel size of the μ-XCT tests was 15.1 μm.

In μ-XCT tests, phases with different X-ray (mass) attenuation coefficients, X(M)ACs, are projected in the images with different gray values. Generally, a phase with the higher density also shows the higher X-ray attenuation, which leads to the lighter color (or the higher gray value) of the phase in the μ-XCT image. It is therefore easy to identify the phase by reading the gray value distributions of the μ-XCT image. For the μ-XCT images of ordinary CBMs, the bright and dark areas, respectively, represent the phases of high density (e.g., unhydrated cement particles or some high-density additives) and low density (e.g., pores) [67].

For compounds, the XAC can be calculated by the mixing rule [68]:

$$XAC = \sum_i w_i (XAC)_i \tag{4}$$

where $w$ is the weight fraction with the subscript i representing the ith component.

The XMACs of some elements, minerals and compounds in CBMs were selectively displayed between 40–120 KeV according to the X-ray energy provided by the X-CT equipment (Fig. 4A and B). The Cu filter attached on the X-ray source tube may filter the low energy X-rays, so the X-rays with the energy over 40 KeV were kept to penetrate the specimens. When evaluating the XMACs of calcium-silicate-hydrate (CSH), the chemical formula of $1.7CaO{\cdot}SiO_2{\cdot}2H_2O$ was adopted. It is clearly shown in Fig. 4A and B that, normally, XMACs are proportional to average atomic number and decrease with photon energy. Clearly, CsCl has the highest XMACs, and as a consequence, can greatly enhance the X-ray attenuation of water with CsCl. It is noteworthy that hydrogen

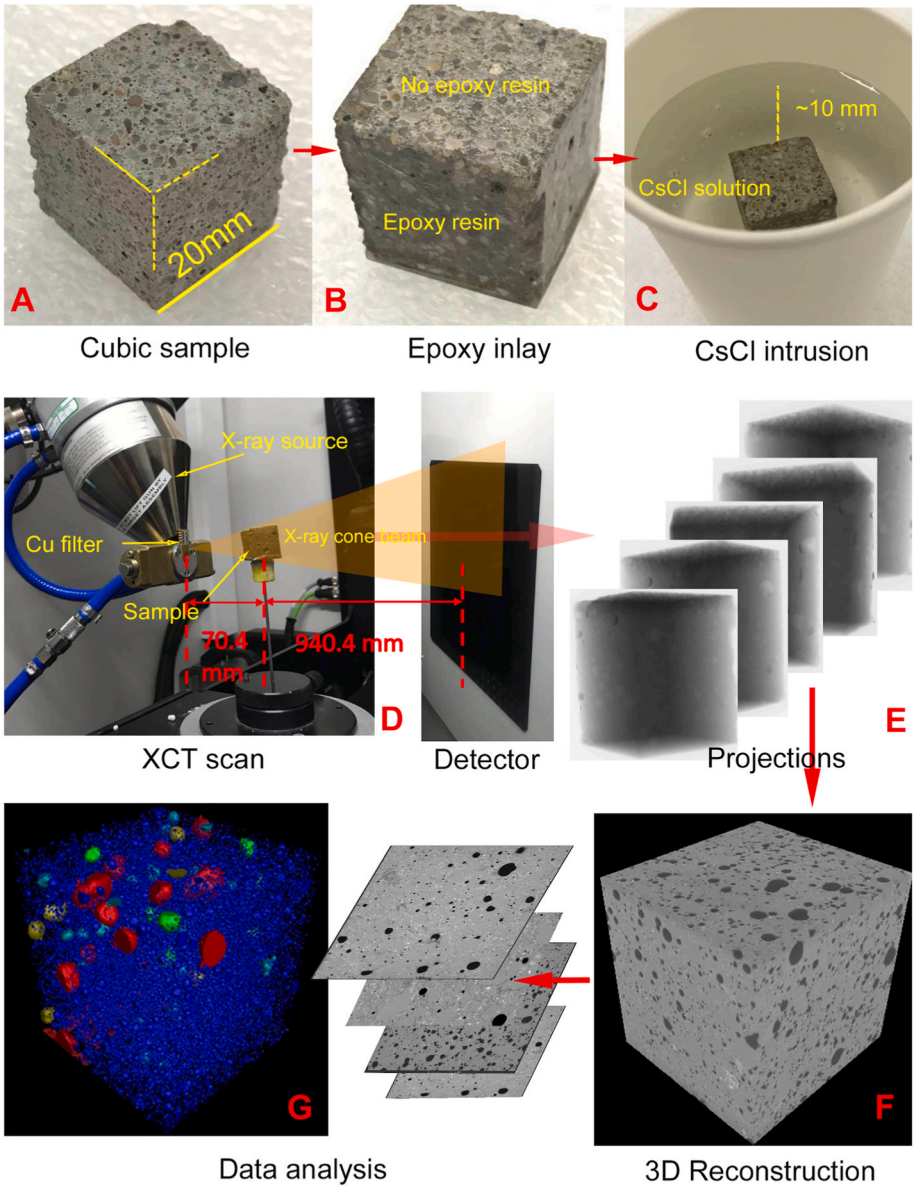


**Fig. 3.** Schematic diagram of testing procedures: (A) fabrication of cubic PMCM specimens (with the edge length of 20 mm); (B) epoxy coating of the side and bottom surfaces leaving the top surface open for water migration; (C) in-situ picture of a ponding test; (D) μ-XCT scans; (E) acquisition of X-ray projections; (F) 3D reconstruction; and (G) phase segmentation and analysis.

shows the higher mass attenuation then that of oxygen between 40 and 120 keV owing to the higher incoherent scattering of hydrogen [68].

### 2.6. SEM/EDS analysis

Scanning electron microscopy (SEM) in the modes of Secondary Electron (SE) and Backscattered Electron (BSE) was applied to measure the microstructure of the mortars after the ponding tests. SE images provide the fracture surface morphology of materials and BSE images provide the compositional information. BSE image analysis requires a relatively complex sample preparation process, consisting of hydration stopping, drying, cutting, epoxy impregnation, grounding and polishing by abrasive papers with various fineness and diamond suspensions in sub-micro size [69]. Energy dispersive X-ray spectroscopy (EDS), that enables the chemical characterization of CBMs' microstructure [38,70], was applied to probe the chemical changes in the mortars caused by the liquid penetration.

For the SE imaging tests, the prism samples were crushed and the inner parts were immersed in absolute ethyl alcohol for 7 d to remove the water confined in the mortars, then the samples were oven-dried at 40 °C for 8 h to evaporate the water-alcohol liquid. The dried samples were coated with platinum to improve the conductivity. For the BSE and EDS tests, the cubic mortars were oven-dried at 40 °C for 24 h once the last X-ray scans completed, and impregnated with a quick-hardening and highly floodable epoxy resin in a cylindrical mould. Later, the solidified resin-covered samples were ground and polished by various grades of sand papers and diamond suspensions with the diamond particle sizes down to 50 nm. After a short carbon coating, the smooth and flat samples were readily prepared for the BSE and EDS tests.

A device of FEI QUANTA FEG 650 ESEM was applied with the voltage of 15 kV and spot size of 3.0 nm for acquiring the SE and BSE images. EDS spectra were tested at the voltage of 20 kV and spot size of 4.0 nm.

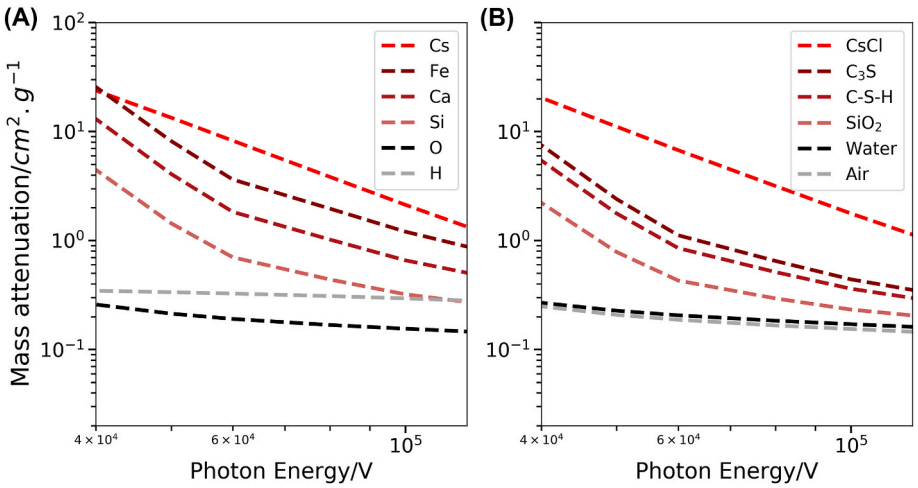


**Fig. 4.** X-ray mass attenuation coefficients of different elements (A) and compounds (B) that may exist in cement versus photon energy range from 40 keV to 120 keV [68].

## 3. Results and discussions

### 3.1. Material strengths

Mortars with 10 wt% SBR or EVA were tested at 1, 3, 7 and 28 d to evaluate the compressive and flexural strengths (Fig. 5). Obviously, the addition of either SBR or EVA in cement mortar can drastically decrease the compressive and flexural strengths of PMCMs. At 1 d, the compressive strength decreases from 16.6 MPa for the reference mortar to 12.1 MPa (73.5%) for the SBR mortar, and to 10.4 MPa (62.7%) for the EVA mortar (Fig. 5A and B). While the compressive strength rises substantially with curing age, SBR and EVA always show the adverse effects. Specifically, the relative compressive strengths of the SBR mortar to the reference mortar is 70.4%, and that of the EVA mortar to the reference mortar is 62.9% (Fig. 5B).

Similar to the data of compressive strength, the flexural strength increases with curing age and decreases with the addition of the polymers into the cement matrix (Fig. 5C and D). The rising rate of flexural strength seems to be slower than that of compressive strength after 3 d (Fig. 5C). Furthermore, the adverse effects on the flexural strength are much lighter than those on the compressive strength. At 28 d, the flexural strengths of both the SBR and EVA modified mortars are approaching 85% of the reference mortar (Fig. 5D). Similar trends on the strength development induced by the incorporation of polymers into CBMs have been reported elsewhere [71]. The adverse effects of the polymers on both compressive and flexural strengths are caused by the formation of a microstructure with more non-connected porosity showing weaker interactions between aggregates and cement matrices (see section 4 for profound discussion).

### 3.2. Mass gain and sorptivity

Fig. 6A shows the mass gains of the mortars *versus* the square root of the immersing time. Clearly, the EVA and SBR mortars show much lower mass gains than the reference mortar during the liquid penetrations. The calculated mass sorptivity (identical to the slope of the $\Delta w$-$t^{0.5}$ plot) is shown in Fig. 6B. The mass sorptivity of the mortars to the CsCl solution is systematically higher than that to the pure water. This is indeed caused by the alterations in the physical properties (density, surface tension and dynamic viscosity) of water by the addition of CsCl. The mix

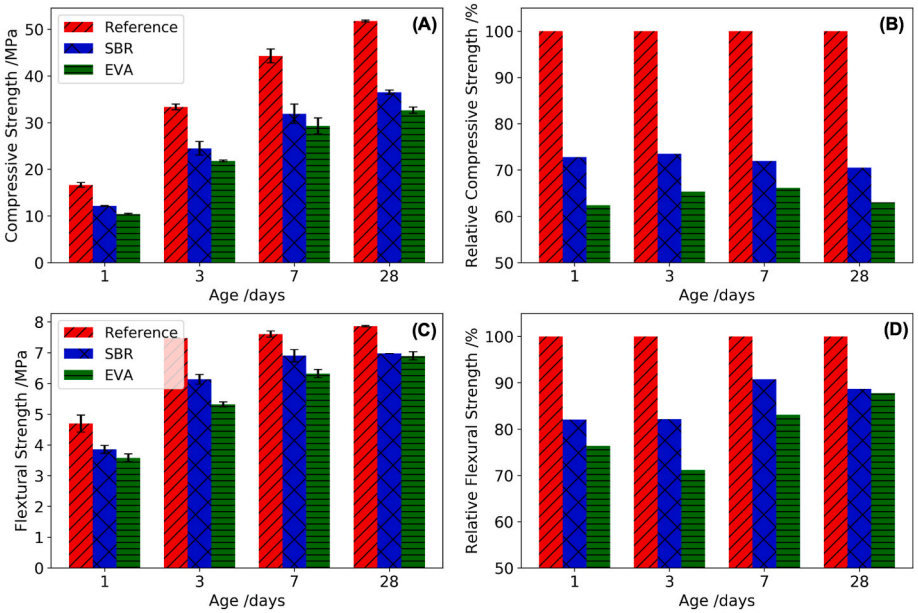


**Fig. 5.** The compressive strength (A), relative compressive strength (B), flexural strength (C) and relative flexural strength (D) of the reference mortar and PMCMs.

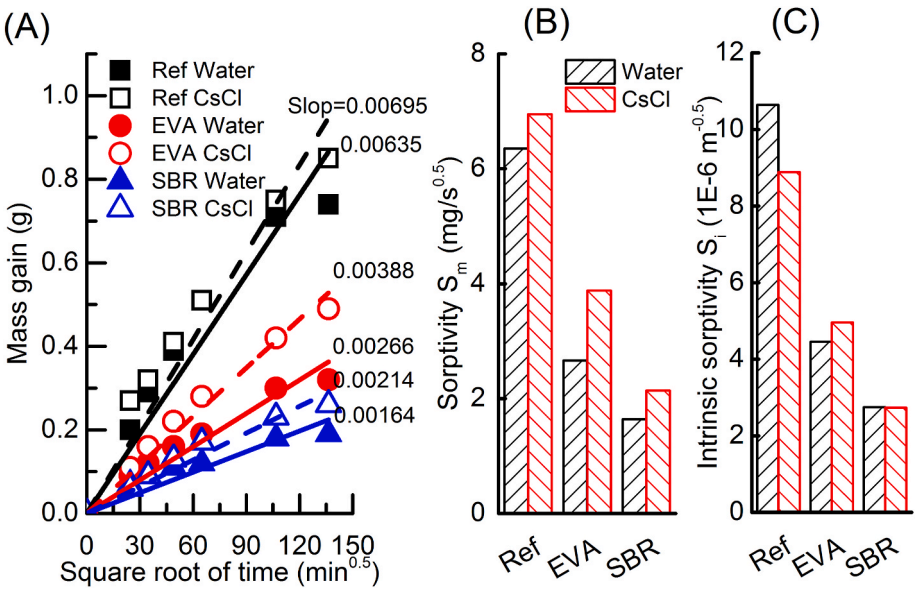


**Fig. 6.** (A) Mass gain of the cement mortars immersed in pure water and CsCl solution and the linear fittings of $\Delta w$-$t^{0.5}$, (B) the mass sorptivity (slope of the fittings in (B)), and (C) the intrinsic sorptivity after the corrections in density, surface tension and dynamic viscosity (Eq. (3)).

of water with CsCl will increase the density and surface tension of the liquid but decrease the dynamic viscosity [72]. At the concentration of 30 wt%, the density, surface tension and dynamic viscosity of the CsCl solution are 1213 (kg/m$^3$), 75.57 (mN/m) [72] and 1.162E-3 (Pa·s) [73], respectively.

After the corrections in density, surface tension and dynamic viscosity, the intrinsic sorptivity was evaluated (Fig. 6C). It shows the similar intrinsic sorptivities between the mortars absorbing the pure

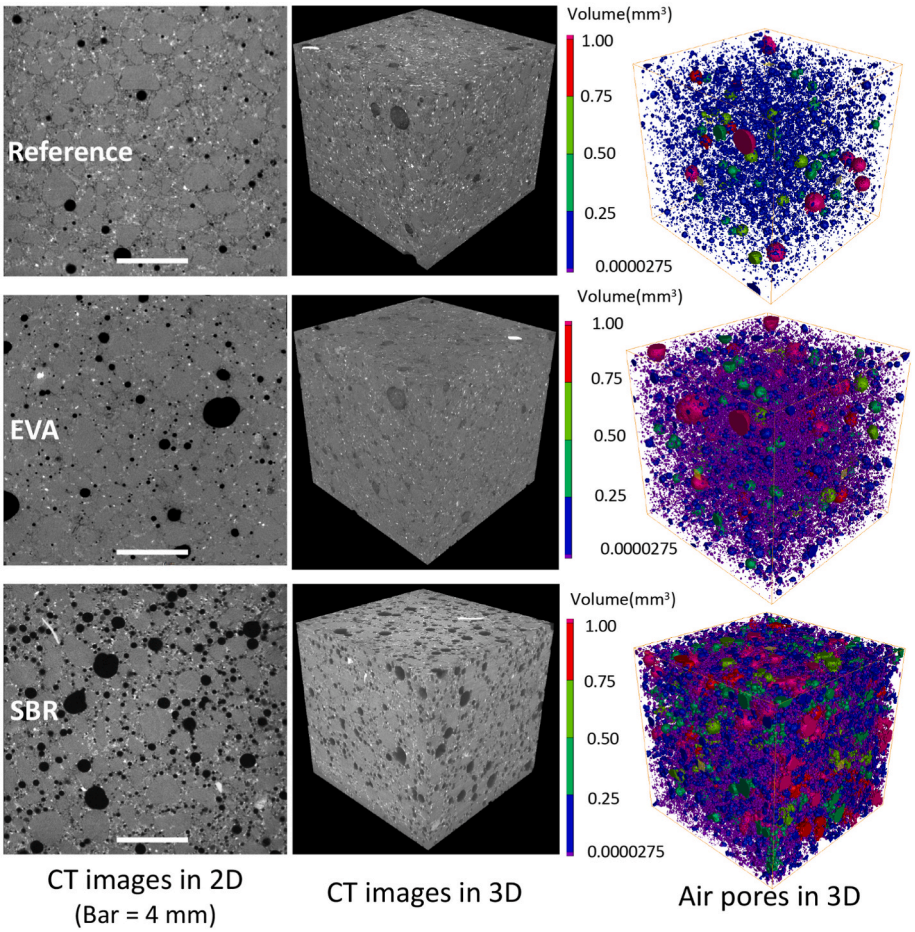


**Fig. 7.** μ-XCT images of the reference (top), EVA (middle) and SBR (bottom) mortars (left: 2D images, middle: 3D images, right: pores in different sizes after segmentation) (the scale bars represent 4.0 mm).

water and those absorbing the CsCl solution. Similar findings were reported in a recent study by molecular dynamic simulations [74], which demonstrated the superimposed capillary imbibition profiles of water and CsCl solutions in a porous C–S–H phase. The intrinsic sorptivity of the reference mortar is around $1 \times 10^{-6}$ $m^{0.5}$, with the addition of EVA and SBR, it reduces by 55% and 70%, respectively (Fig. 6C). The results tell that both EVA and SBR can greatly improve the resistances against water penetration in the ponding tests. This is due to the microstructure modifications provided by the polymers and their interactions with the cement hydrates and aggregates.

### 3.3. Pore structure characteristics by μ-XCT

The effects of EVA and SBR on the pore structure of mortars were investigated by μ-XCT. Fig. 7 shows the selected 2D, 3D and pore phase images of each mortar, where the size of the region of interest (RoI) is 3375 $mm^3$. The light phases in the 2D and 3D μ-XCT images represent the detectable unhydrated cement particles with the higher X-ray attenuation, and the dark circles denote the air voids and/or pores isolated in the mortar matrices with the lower X-ray attenuation (Fig. 4b). It is obvious that the PMCMs contain more pores than the reference mortar (Fig. 7). The air voids are heterogeneously entrained in the reference mortar matrix (Fig. 7(top-right)). While increasing the air content, EVA seems to enhance the spatial heterogeneity of the air voids (Fig. 7 (middle-right)). The blend of 10% SBR promotes both the content and size of the air voids (Fig. 7(bottom-right)).

It is difficult to single out the sand grains from the cement pastes with/without the polymers, because they show the similar gray values. Therefore, the sand grains and pastes were integrally treated as the solid skeleton in the μ-XCT analysis. Indeed, when reading the gray value histograms (GVHs) of the mortars in a volume of interest (VoI), one can find dual peaks: the first peak with the lower gray values captures the air voids/pores, and the second peak with the higher gray values denotes the solid skeleton (Fig. 8A). Because of the limited content of the unhydrated cement particles, it is rather difficult to form a peak in the GVHs (Fig. 8B).

To quantify the pore structure changes caused by the polymers, some characteristic pore parameters (i.e., total porosity, pore number, pore diameter, sphericity and compactness) were statistically analyzed based on the pore data from the μ-XCT tests. Here, the total porosity only counts the pores larger than 8 voxels (27543 $\mu m^3$). Sphericity is defined as the ratio between the surface area of an ideal sphere ($A_{sph}$) and that of a pore ($A_p$) with the same volume (sphericity $= A_{sph}/A_p$). Compactness is expressed as the ratio between the volume of a pore ($V_p$) and that of its circumscribed sphere ($V_{sph}$) (compactness $= V_p/V_{sph}$). Values of both the sphericity and compactness are between 0 and 1, measuring the extents by which a pore body deviates from an ideal sphere. The higher is the sphericity (or compactness), the closer are the pores to the ideal spheres.

Fig. 9 shows the selected pore parameters of the mortars. The porosity of the reference mortar is 4.33%, greatly lower than that of the cement mortar with the same w/c ratio determined by other porosimetries (e.g., mercury intrusion porosimetry, gas sorption and NMR [75,76]) due to the limited pore sizes detected by the μ-XCT tests. When EVA and SBR are added into the mortar, the total porosity is dramatically increased from 4.33% to 8.03% and 21.36%, respectively (Fig. 9A). This is caused by the air entraining effect of the polymers [77–79]. Fig. 9A shows that SBR has much greater air entraining effect than EVA. The air entrainment effect of the polymers also increases the pore numbers (Fig. 9B). Statistical analysis shows that EVA can slightly decrease the mean pore diameter (Fig. 9C) because more pores below 0.4 mm are generated (Fig. 9F). By contrast, SBR can significantly depress the number of the pores thinner than 0.1 mm but increase the pores between 0.2 and 0.6 mm (Fig. 9F), so the porosity, pore number and mean pore size all rise significantly (Fig. 9A–C). Polymers' addition always increases the mean sphericity and compactness of the pores (Fig. 9D and E), and EVA shows the greater increasing effects on pore sphericity and compactness than SBR. The histogram plots (Fig. 9G and H) clearly display the details in pore sphericity and compactness. The heavily increased porosity and the pore geometries induced by the polymers account for the significant strength decreases shown in Fig. 5.

### 3.4. Diagnosis of water penetration by μ-XCT images

When CsCl solution is used as the liquid to invade the open pores of cement mortars, some distinct features can be extracted from the μ-XCT data, which can help diagnose the liquid penetration depths and fronts in the materials. As an example, Fig. 10 shows the μ-XCT images and GVHs acquired from a reference mortar specimen after the ponding action for 40 min. Obviously, the invasion of the CsCl solution into the mortar can be visually probed from the μ-XCT image (Fig. 10A). The rises of X-ray attenuation of the phases filled with the CsCl solution, i.e., the cement paste matrix and the interfacial transition zone (ITZ) between cement matrix and aggregates, greatly enhance the contrast of the X-CT images. This feature can facilitate the diagnosis of the penetration depths (see below for more details).

Cross-sectional views of the mortar slices beyond, on and in the penetration fronts provide more evidences. For the un-penetrated part, the macro air pores (dark circles) are distinguishable (Fig. 10B) and the corresponding GVH peak (at the gray value around 30/255 for 8 byte 2D gray scale image) is tiny but conspicuous (Fig. 10C). The aggregates and cement pastes share the remaining spaces with the similar gray values, which therefore greatly raises the intensity of GVH peak (at the gray value around 100/255) (Fig. 10C).

Once the open pores are partially or fully saturated with the CsCl

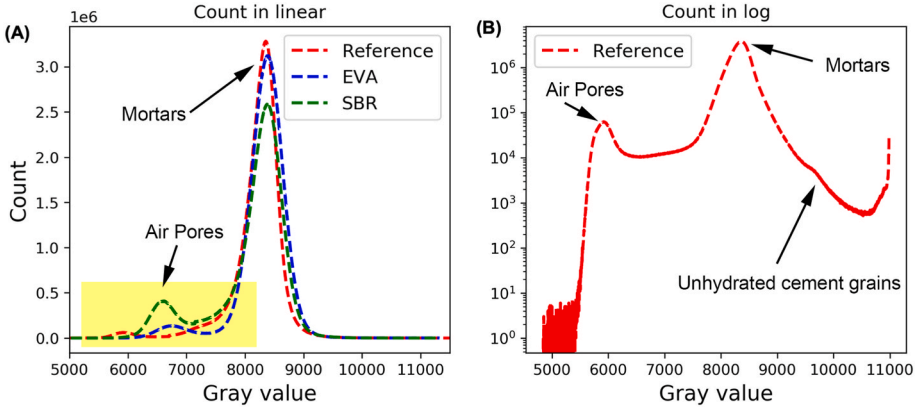


**Fig. 8.** (A) GVHs of the reference, EVA and SBR mortars showing obvious two peaks denoting the pores and solid skeletons, and (B) the logarithm GVH of the reference mortar showing an unobvious peak representing the unhydrated cement particles.

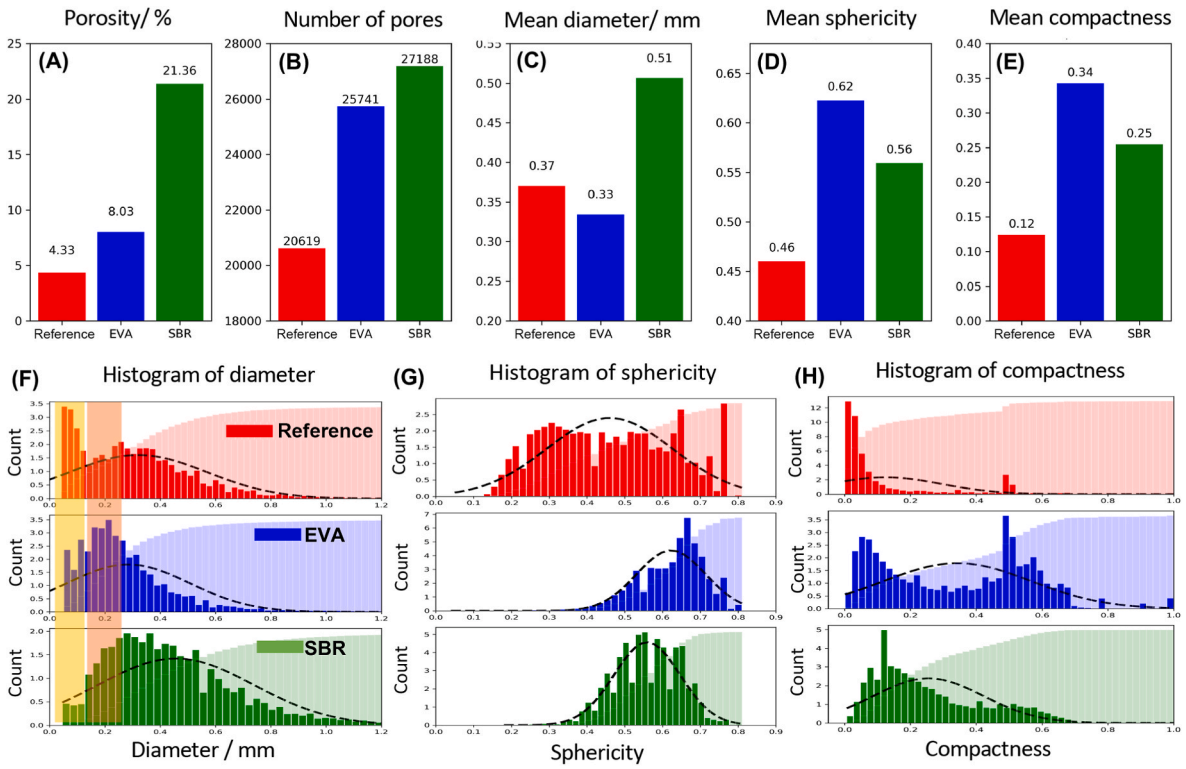


**Fig. 9.** Pore characteristics of the reference, EVA and SBR modified mortars: (A) porosity, (B) pore number, (C) mean diameter, (D) mean sphericity, (E) mean compactness, and distribution histograms of (F) diameter, (G) sphericity, (H) compactness.

solution, both the X-ray attenuation images and GVHs are significantly changed. As shown in Fig. 10D and F, the pastes containing CsCl appear to be much brighter, whereas the air voids and aggregates keep the color in the images because they are unlikely to absorb the CsCl solution during the ponding tests. For the mortar slice on the penetration fronts (Fig. 10D), some areas are brighter, some are not, which are the consequence of the un-even penetration of the CsCl solution in the material. One thus can trace the paths and fronts of liquid penetration by reading the color (or gray value) changes in the μ-XCT images.

For the mortar slice in the penetration fronts, the cement paste (and the ITZs) are dyed due to the fillings of the CsCl solution in the pores, so one can easily distinguish the pores, aggregates and cement pastes in the μ-XCT image (Fig. 10F). The dyeing of the cement paste is induced by the greatly increased X-ray attenuations of the CsCl solution saturated paste, and consequently, the gray values are increased. Specifically, the average gray values of Fig. 10C, E and 10G are 103.0/255, 124.4/255 and 134.1/255, respectively. Note that the gray values of the air voids and aggregates stay nearly unchanged at around 30/255 and 100/255, respectively, which truly tells that no liquid penetration occurs in those phases. The rises of gray values of the cement matrix saturated with the CsCl solution generate the third GVH peak (at the gray value around 160/255) (Fig. 10G). It is expected that the X-ray attenuation enhancement may also provide a way toward quantitatively characterizing the aggregates by μ-XCT tests since the paste phase can be dyed by the penetration of CsCl solution.

### 3.5. *Water penetration processes as viewed from μ-XCT*

Fig. 11 demonstrates the selected μ-XCT images of the mortars during the immersion tests from 0 to 310 min. The bright areas represent the cement paste filled with the CsCl solution, whereas the dark-gray areas represent the originally non-penetrated areas. Images at the same position were carefully aligned, so the intrusion process can be vividly observed. The contrast gradients in the μ-XCT images of the CsCl penetrated mortars are obvious, and the liquid penetration fronts can be directly drawn (see the dashed lines in Fig. 11). It seems that the liquid penetration fronts are not strictly horizontal, meaning that the liquid intrusion speed is un-even due to the heterogeneous mortar microstructure. The liquid is more likely to penetrate along the porous paths along the ITZs between cement matrix and aggregates. The air voids are sealed to prevent the liquid penetration. Akin results were reported elsewhere [80].

The occurrence of liquid invasion begins immediately after the mortar cubes are immersed into the liquid. This initial water intrusion is particularly obvious for the reference mortar. For example, after the first ponding test for 10 min, the intrusion depth is around 3 mm. As the intrusion time is prolonged to 20, 40, 70, 190 and 310 min, the intrusion depths are raised to around 4, 5, 6, 9 and 14 mm, respectively (Fig. 11Top). After the ponding test for 5 h, around two-thirds of the reference mortar cube has been penetrated by the CsCl solution (the quantitative assessment of penetration depth was given in section 3.6).

The liquid penetrations in the materials slow down in the PMCMs. Specifically, the penetration depths at 310 min are around 5 and 3 mm for the EVA and SBR mortars, respectively (Fig. 11Middle and Bottom). It is clear that the SBR mortar shows the higher water penetration resistance than the EVA mortar. At 10 min, the liquid intrusion in the SBR mortar is rather superficial. The penetration speed is so slow that it requires 190 min to cross a superficial aggregate (with the size around 1.5 mm) in the upper left corner of the SBR mortar (see the rectangles in Fig. 11).

Fig. 12 shows the 3D images of a SBR mortar at different ponding times, which demonstrate how the liquid goes around an aggregate. Clearly, the liquid first tends to enter the ITZ around the aggregate. However, due to the improvement in microstructure of the ITZ and cement matrix by SBR (so does EVA; see section 4 for more microstructure evidences), the liquid invasion is greatly obstructed. The results of Figs. 11 and 12 visually prove the barring effect of EVA and SBR against water penetration through mortars.

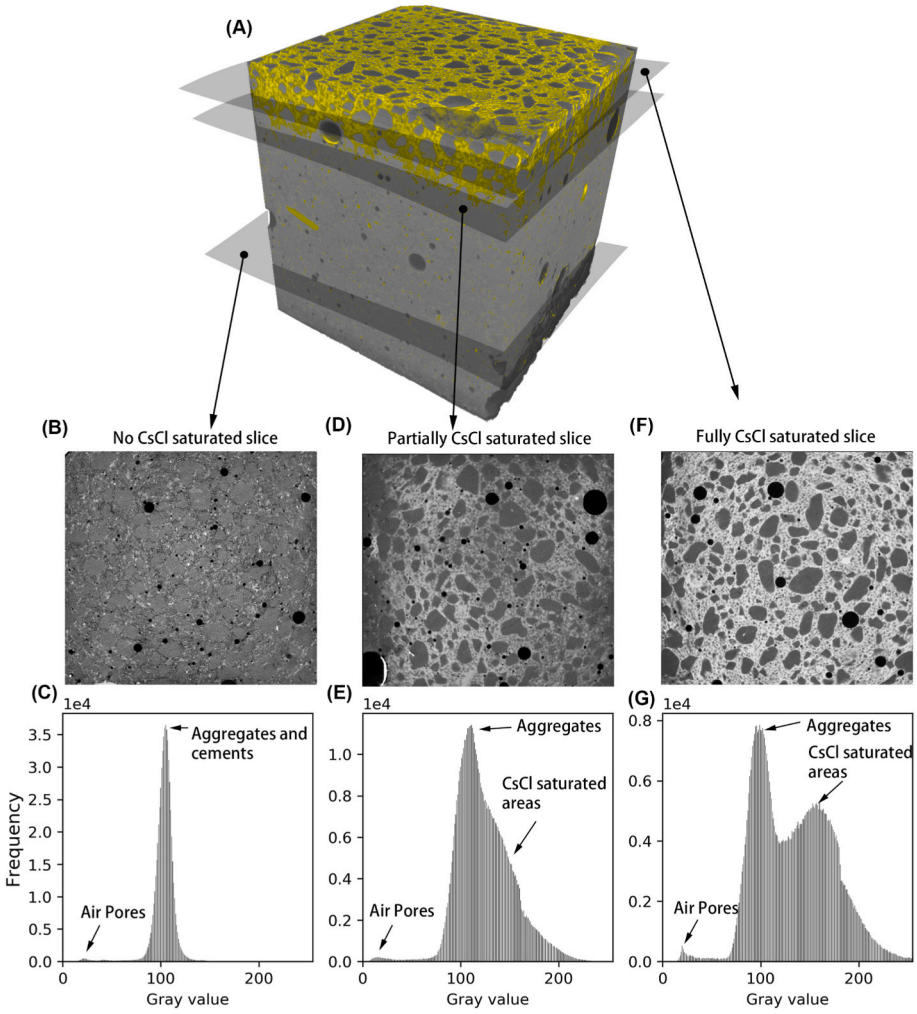


**Fig. 10.** Representative demonstration of μ-XCT results of the reference cement mortar under the ponding action of the CsCl solution for 40 min: 3D image after phase segmentation (yellow: the cement matrix and ITZs filled with the CsCl solution) (A); 2D sectional image near the bottom showing no CsCl penetration (B), that on the liquid penetration fronts showing partial CsCl penetration (D), and that near the top surface showing full CsCl penetration (F); (C), (E) and (G) represent the gray value distributions of the 2D images (B), (D) and (F), respectively. (For interpretation of the references to color in this figure legend, the reader is referred to the Web version of this article.)

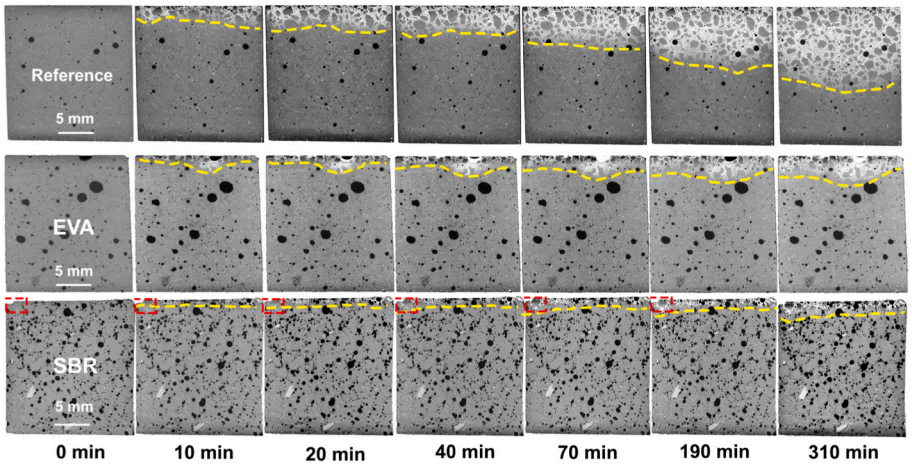


**Fig. 11.** Time evolution of μ-XCT images of the reference (Top), EVA (Middle) and SBR (Bottom) mortars (For each mortar, the same vertical sections at different times were chosen to indicate the liquid penetration process; the dashed lines roughly show the penetration fronts; and the rectangles on the top left corner of the SBR mortar capture a local aggregate discussed in Fig. 12).

### *3.6. Water penetration dynamics as viewed from gray value distribution*

Because of the un-evenly distributed water penetration fronts caused by the mortar heterogeneous microstructure; it is difficult to quantify the penetration depths by directly reading the images shown in Fig. 11. A gray-value dependent method was therefore developed in this work. The method was inspired by the changes in GVHs of the mortars with the immersion time. Fig. 13 shows the voxel-gray value spectra of the reference, EVA and SBR mortars. As the immersion time increases, the peak intensities of the solid skeletons (aggregates plus non-penetrated

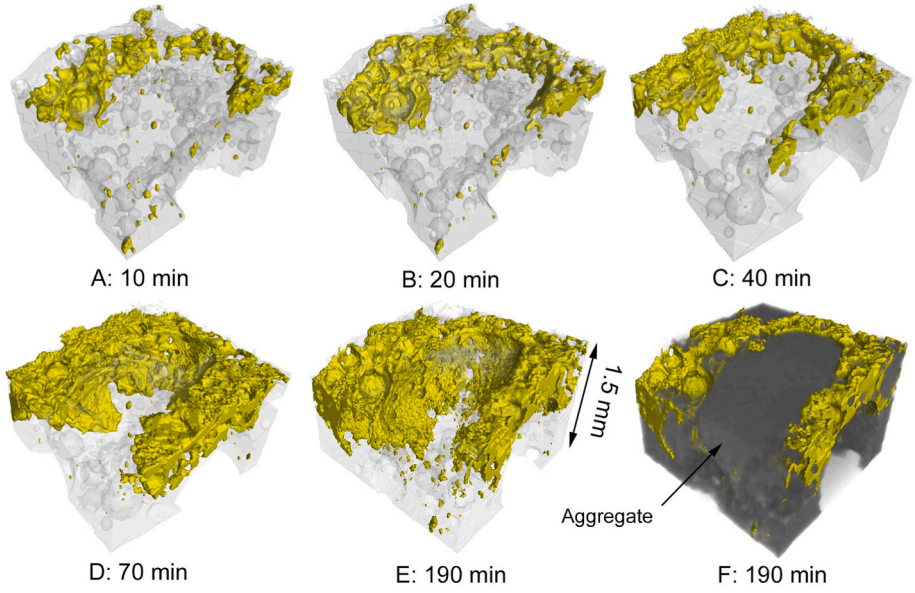


**Fig. 12.** 3D μ-XCT images showing the invasion processes of the CsCl solution around an aggregate near the exposing surface of the SBR mortar at 10, 20, 40, 70 and 190 min (A–E) (the yellow phase represents the liquid-penetrated cement paste). The aggregates were set to be transparent and opaque in sub panels E and F, respectively. (For interpretation of the references to color in this figure legend, the reader is referred to the Web version of this article.)

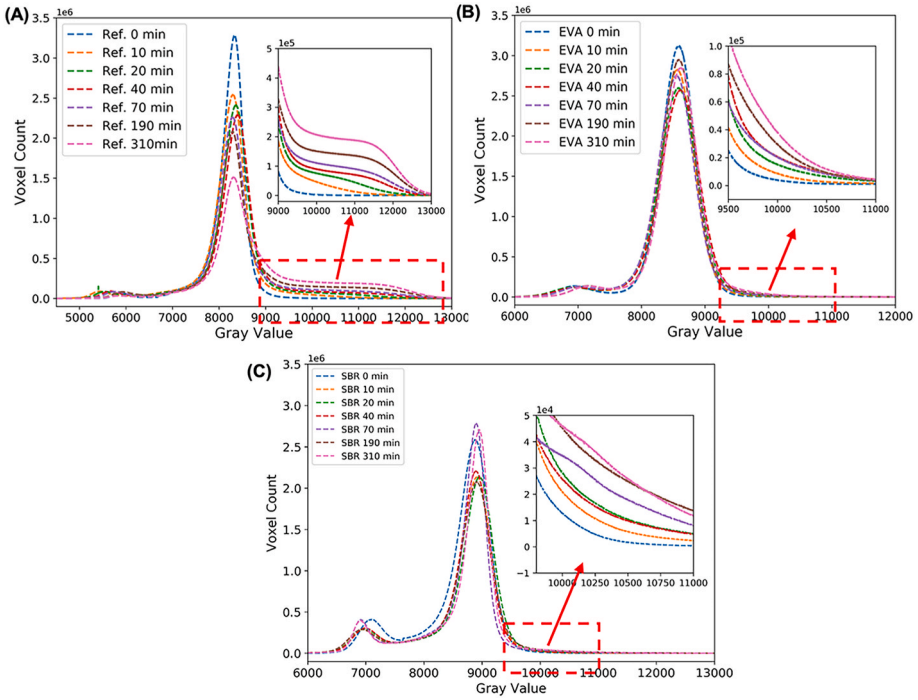


**Fig. 13.** Comparative plots of voxel-gray value spectra of the reference (A), EVA (B) and SBR (C) mortars at different penetration times. The subplots in A, B and C show the rises of the voxel count just over the main peak of gray values with increasing the ponding time.

cement paste) decrease, but those of the cement paste filled with the CsCl solution increase. Due to the limited liquid penetrations in the EVA and SBR mortars, the rises of the voxel-gray value spectra at the region of high gray values are relatively minor (see the subpanels in Fig. 13B and C).

To obtain the intrusion depth, we acquired the horizontal slices of the μ-XCT images (800 slices in 20 mm with the thickness of 25 μm per slice) and analyzed the gray values of those slices from the surface to the bottom along the intrusion direction. The average gray values (AGVs) of each slice were calculated, and the AGV distributions along the penetration direction for all mortars are shown in Fig. 14A–C. Here, the Y-axis represents the slice position, the top surface of the sample, where the liquid intrusion begins, was set as 0. The AGV spectrum of the mortar before liquid penetration was set as the baseline to quantify the AGV changes. As shown in Fig. 14, the AGV baselines are un-even in different slice positions. For example, the AGVs near the top and bottom surfaces are significantly lower than those of the inner part. This may be because the surface mortars contain more cavities caused by the spalling of aggregates during cutting. When CsCl solution enters these cavities, the AGVs rise significantly, which explains the AGV oscillations near the top

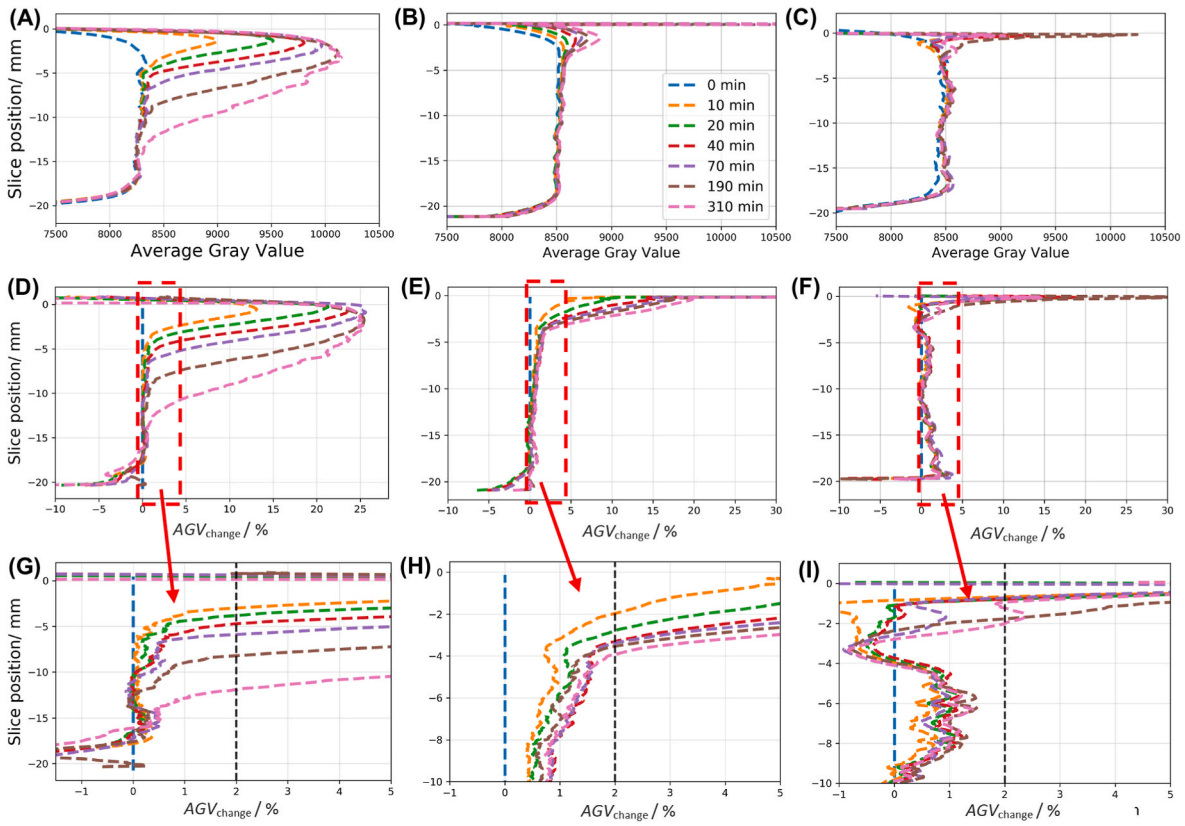


**Fig. 14.** AGV spectra of the reference (A), EVA (B) and SBR (C) mortars and the changes in AGV (D–F). Sub panels (G–H) show the magnified changes in the AGV spectra between −1% and 5%. The 2% change of the AGV spectra was set as the threshold value for identifying the average water penetration depths (black dashed lines in sub panels G–H).

surface (Fig. 14B and C). As the immersing time increases, the AGVs near the top surface rise obviously owing to the continual liquid invasion. As the position deepens, the AGVs slowly merge with the baselines.

The AGV changes were calculated by $\Delta AGV = (AGV_t - AGV_0)/AGV_0 \times 100\%$, where $AGV_t$ and $AGV_0$ are the AGV of a slice after the liquid immersion for $t$ min and the baseline AGV before the immersion, respectively. The $\Delta AGV$ spectra along the depth are displayed in Fig. 14D–F. Clearly, sharp gradients in AGV change can be found, and the magnified plots are illustrated in Fig. 14G–I. The results imply that the AGV plots are sensitive to the invasions of the CsCl solution. This method was also employed to identify the imbibition depth of ethanol in a cement paste [81]. In this work, $\Delta AGV = 2\%$ was adopted as the threshold value to evaluate the penetration depths. It means that the slices with $\Delta AGV$ less than 2% are classified as the unpenetrated area.

The liquid intrusion depths ($\Delta h$) obtained by the threshold segmentation are shown in Fig. 15A. Resembling the observations displayed in Fig. 11, one may find out that the reference mortar always has the greatest penetration depths, and the polymer modifications can

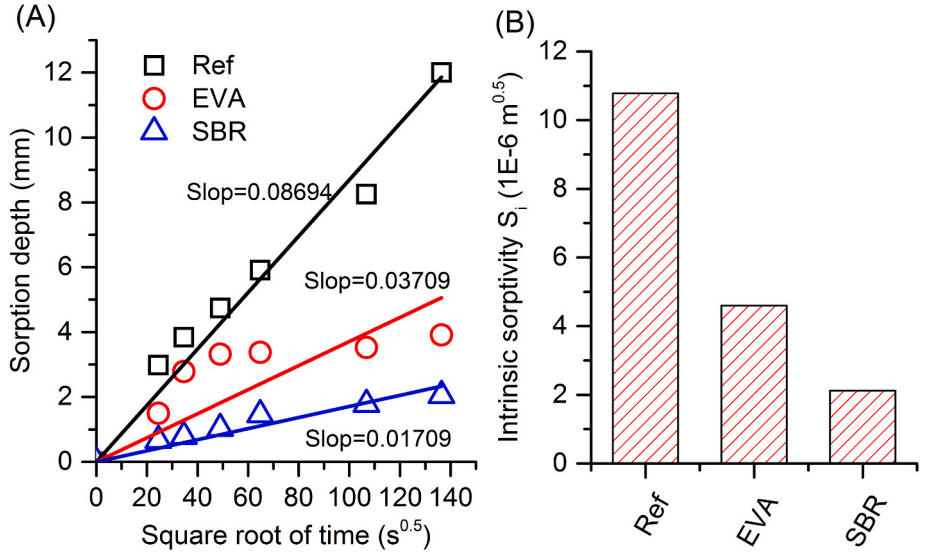


**Fig. 15.** (A) Penetration depths of the Reference, EVA and SBR mortars and (B) the intrinsic sorptivity calculated through Eq. (3).

profoundly resist the liquid penetration. The SBR mortars show the greatest water penetration resistance. For example, the penetration depths of the EVA and SBR mortars at 310 min are close to those of the reference mortars at the ponding time for 20 and 10 min, respectively. The intrinsic sorptivity, calculated from Eq. (3), is shown in Fig. 15B. The values of intrinsic sorptivity are similar to those calculated from the mass gain data (Fig. 6C). This suggests that the AGV-based penetration depths are reliable.

## 4. SEM-EDS analyses and discussions on the anti-water mechanisms

### 4.1. Microstructure

Fig. 16 shows the SE images of representative phases and sites of the mortars in different magnifications. At a low magnification, it is difficult to find out the morphological differences between the reference, EVA and SBR mortars (Fig. 16A–C), mainly owing to the similar compactness of the material matrices. The similar compactness in turn explains the similar gray values of the mortar skeletons displayed in Figs. 12 and 13.

Local sites in the mortars were measured to explore how the polymers impact the mortar microstructure. For the reference mortar, the amorphous CSH gels maturely grow around the cement grains to diminish the inter-particle gaps (capillary pores), and numerous needle-like ettringites (AFt) nucleate and grow between the gaps (Fig. 16D). These capillary gaps may interconnect to form continually percolated 3D pore clusters, facilitating water penetration. The expected large-scale plate-like calcium hydroxide (CH) crystals are not found between the gaps but around an air void (Fig. 16J).

The micro morphologies of the hydration products in the PMCMs are different with those in the reference mortar. The presences of polymers in cement mortar may alter the hydration products and their microstructure. On one hand, the formation and growth of CSH, CH and AFt are drastically constrained by the obstructing effect of the polymer films (Fig. 16E and F). Our previous study [38] implied that polymers can form films on cement grains to decrease the dissolution of reactive minerals, the migrations of ions and water molecules, and the nucleation and growth of hydration products during cement hydration. On the other hand, the gaps between cement particles can be filled with polymer particles and films, which play important roles on anti-water properties.

Polymers also alter the ITZs between cement matrices and aggregates (Fig. 16G, H and I). Owing to the relatively low mechanical properties and porous microstructure of ITZs, it has long been considered as the weak phase in CBMs to lower the material strength [82,83] or to raise the permeability [84]. This viewpoint can be supported by the porous microstructure of ITZs for the reference mortar shown in Fig. 16G. When EVA or SBR is blended with cement mortar, polymer films can absorb onto the surfaces of aggregates and may partially fill the pores in ITZs (Fig. 16H and I). In this regime, the water invasion of the ITZs can be

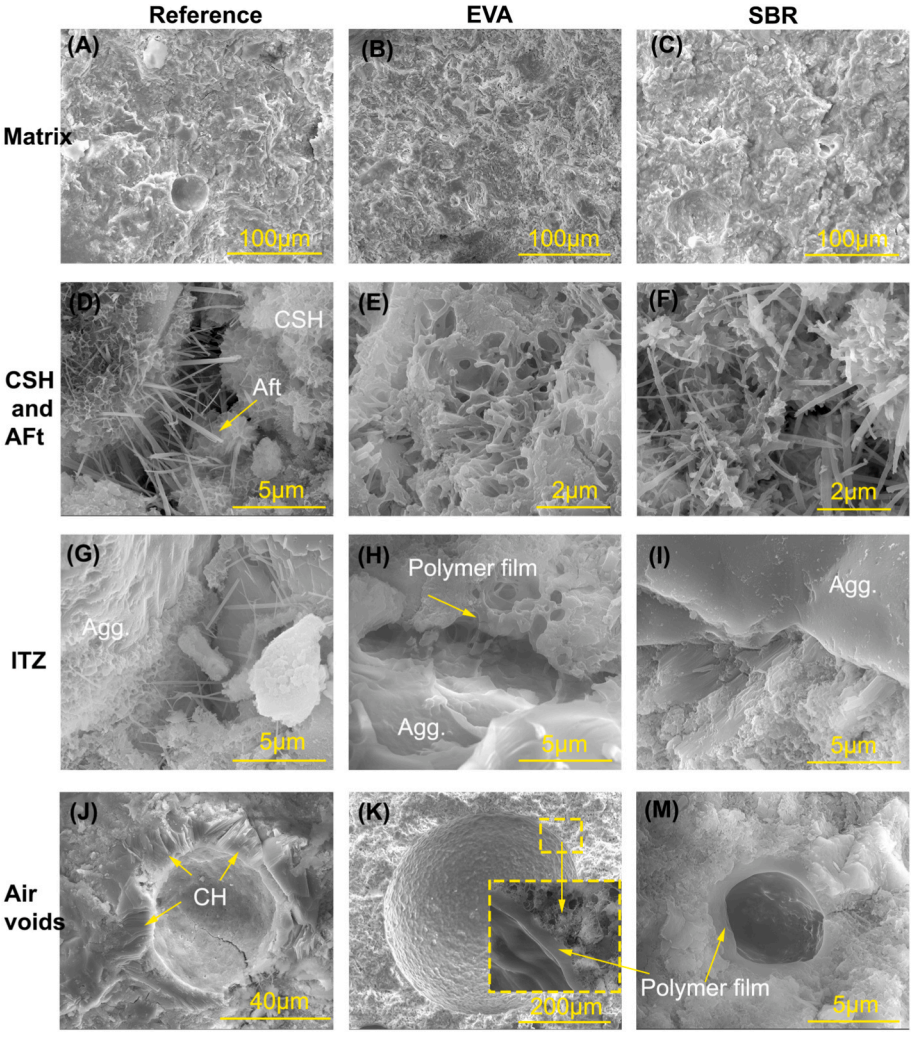


**Fig. 16.** SEM images of the mortars: Columns from left to right: reference (A, D, G, and J), EVA (B, E, H and K) and SBR (C, F, I and M) mortars; rows from up to bottom: mortar matrix (A–C), C–S–H gel and AFt (D–F), ITZ (G–I) and air voids (J–M).

greatly prevented.

SEM tests also help unravel the role of polymers on the formation of air voids. As displayed in Fig. 2, polymer particles can coalescence together to form continually connected films when the excess water is dried or consumed by cement hydration. If the air is entrapped in the films, polymer balloons will form, and those balloons would be the parents of the air voids in cement mortars. As clearly shown in Fig. 16J–M, the surfaces of the air voids in the PMCMs are covered with a layer of polymer film. Because the particle size of EVA is much larger than that of SBR (Table 2), the film thickness and the air void size in the mortar modified by EVA is much larger than that those by SBR. The entrained air pores result in the higher porosities (Fig. 9) and lower mechanical properties (Fig. 5). When regarding to porosity and strength, SBR can introduce more pores and thus bring the severer strength loss to the mortars than EVA. The films around the air voids seem to be impermeable to water.

### 4.2. Trace of Cs in ITZ by BSE-EDS

The microstructure of some randomly chosen ITZs was detected by BSE and the element distributions were tested by EDS mapping and line scans. Because the element with a higher atomic number also shows a higher backscattered electron emission coefficient, CsCl can also enhance the brightness of BSE images [85]. Fig. 17A, D and G show the BSE images of ITZs in different mortars, where the light gray rough surfaces are the cement paste in which the bright areas are the CsCl deposits, the gray smooth surfaces are the aggregates, and the dark gray areas are the resin-filled pores (Fig. 17G). The phase identification is supported by the element tests shown in Fig. 17B, E and 17H. Roughly, the CsCl deposits are homogeneously distributed around the aggregates for the reference mortar (Fig. 17A), while for the EVA and SBR mortars, the CsCl deposits are un-evenly distributed in the cement pastes and are not directly in contact with the aggregates (Fig. 17D and G). This may tell that the less CsCl solution permeates along the surfaces of the aggregates in the PMCMs. The element mapping images (Fig. 17H) evidence the un-even distributions of Cs and Cl in the pastes around the aggregates for the SBR mortar sample.

Chemical binding may occur between the elements (Cs and Cl) and C–S–H gels (and other minerals) in CBMs [86–89]. In this work, the physical sorption of CsCl, in the ITZ gaps and the pores in hydration products, like CSH gels, may account for its abundant distribution in the paste. A close examination on the Cs and Cl mapping images of the SBR mortar tells that the brightest spots (Fig. 17H) coincide with the CsCl deposits detected by BSE (Fig. 17G). EDS line scans show the significant changes of Ca and Si on the interface between the cement paste (CSH, CH and other minerals) and the aggregates (quartz). The shifts of Cs and Cl are sharp for the reference mortar but mild for the PMCMs, when the EDS detector scans from an aggregate to the surrounded paste (Fig. 17C, G and 17I). The ITZ size evaluated from the element spectra by EDS scans (see the shadowed areas in Fig. 17C, G and 17I), again, testifies the heterogeneous microstructure of the PMCMs.

Overall, the BSE and EDS results tell that the deposition of CsCl in the ITZs of the PMCMs is constricted, because EVA or SBR can block the open pores against liquid penetration.

### 4.3. The anti-penetration mechanisms of PMCMs

From the integrated experimental analyses shown above, the anti-penetration mechanisms of PMCMs can be elucidated. The anti-penetration effects are initiated from the hydration process of PMCMs. For the reference mortar, four main elements (i.e., cement particles, aggregates, water and the entrained air voids) constitute the fresh mortar (Fig. 18A1). As hydration proceeds, hydration products (mainly CSH, CH and AFt) nucleate and grow somewhere, consuming water and partially filling the inter-particle spaces that are initially occupied by the water (Fig. 18A2). The ubiquitous presence of the inter-particle spaces (especially for the spaces between cement grains and aggregates) can provide the penetration channels for water and other media (Fig. 18A3). In this regime, water can rapidly penetrate into 12 mm in 310 min as probed by μ-XCT (Figs. 11 and 15).

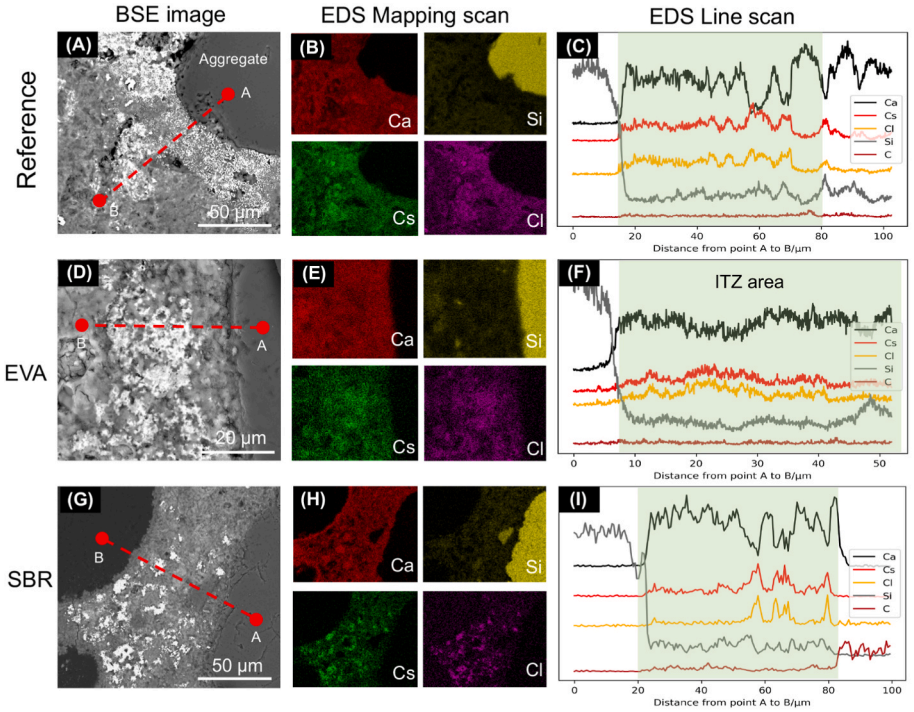


**Fig. 17.** BSE images (A, D and G) and EDS mapping (B, E and H) and line scan (C, F and I) results of the reference (A–C), EVA (D–F) and SBR (G–I) mortars. The dash lines from A to B in the subpanels A, D and G show the EDS line scanning positions and directions; the shadowed areas in the subpanels C, F and I represent the size of ITZs.

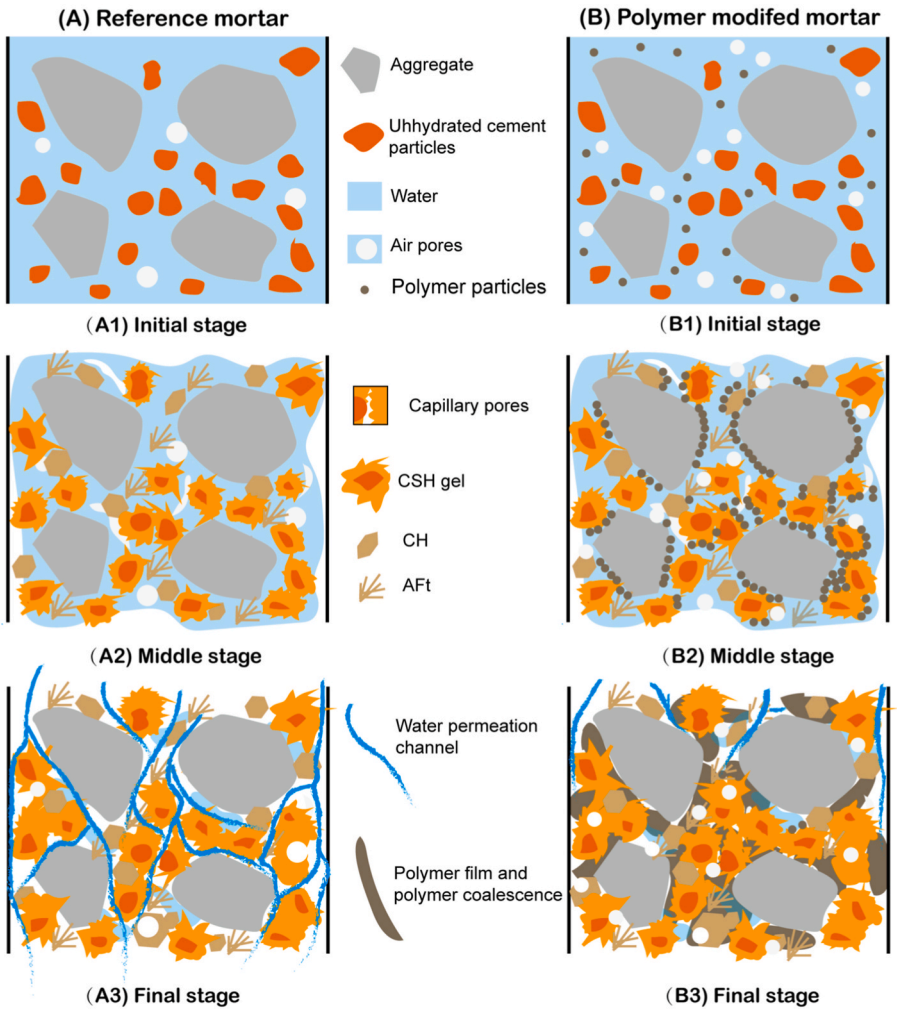


**Fig. 18.** Sketches of 3-stage hydration processes of the reference mortar (A) and PMCMs (B) (The scales of the phases are modified for schematic illustrations).

Hydration processes are altered when polymers are mixed with cement mortar. Polymer emulsion, a highly floodable suspension, partially replaces water to fill the spaces among all particles (Fig. 18B1). During mixing, numerous air voids are introduced into the polymer emulsion and stably entrapped in the hardened material matrix (Fig. 7). Indeed, air-entrainment is an important characteristic of PMCMs [77–79]. Then the polymer particles may precipitate on the surface of the aggregates and cement particles (Fig. 18B2). The partial enclosure of the cement grains by the polymer particles, to some extent, retards the cement hydration [38,90]. When water is progressively consumed by cement hydration, polymer films form and are spatially interconnected (Fig. 18B3). Unlike the inter-particle spaces that provide the penetration channels in ordinary cement mortar, those spaces in PMCMs are partially occupied by the polymer film networks. Therefore, the open channels in the reference mortar for water penetration are partially sealed, shrunk or blocked by the formation of the polymer films or agglomerates (Fig. 18B3), even though the total porosity is increased (Figs. 7 and 9). In this regime, the resistance of liquid penetration into PMCMs can be enhanced by the polymers and their interactions with cement matrix and aggregates (Figs. 10 and 14).

In short, the spatially-connected polymer films make the microstructure of cement mortar more porous but less permeable by obstructing the open channels for mass migration. It is expected that the low permeable PMCMs should also show excellent durability performances related to the transport properties of materials, such as, chloride diffusion, carbonation and gas permeability. The relevant issues deserve rigorous investigations in the future.

## 5. Conclusions

In this work, the anti-penetration of EVA and SBR mortars were in-situ and non-destructively monitored by μ-XCT. Partial surface coating was performed on cubic mortars for ponding tests. CsCl solution was adopted as the penetration liquid, because it can greatly improve the contrast of μ-XCT images while has little impacts on the penetration dynamics of water. SEM/BSE and EDS techniques were applied to characterize the microstructure of the mortars. The following conclusions can be drawn:

(1) Mortars with EVA or SBR show the lower compressive and flexural strengths. The adverse effects on flexural strength are less than those on compressive strength. The causes of the strength decrease are the increases of porosity and the retardation of cement hydration induced by the polymers.
(2) The incorporation of EVA or SBR into cement mortar alters total porosity, mean void size, sphericity and compactness. SBR can more efficiently entrain air voids in cement mortar.
(3) The brightness of the cement paste filled with the CsCl solution is greatly increased, while that of the aggregates and air voids are maintained because the latter two phases do not absorb CsCl. The changes in brightness of the cement pastes before and after CsCl penetration allow us to in-situ trace the liquid penetration fronts by reading the μ-XCT images. The changes in gray value spectra enable the separation of aggregates from cement paste.

(4) A method of counting the average gray value of horizontal slices at different positions was developed. The water penetration depth was quantified by a thresholding method on the AGV changes. Liquid fronts reach 12, 4 and 2 mm for the reference, EVA and SBR mortars at the ponding time of 310 min.
(5) Polymers tend to form continual impermeable films after removing water and introduce massive air voids in cement matrix. Hydration products are impacted by the presence of polymers, and the surfaces of air voids are covered by a layer of polymer film.
(6) CsCl also increases the brightness of BSE images because Cs can enhance the backscattered electron emission coefficient. CsCl is homogeneously detected in the ITZs of the reference mortar, but is heterogeneously probed in the ITZs of the PMCMs.
(7) Polymers can greatly increase the anti-penetration of cement mortar by blocking the channels for liquid migration. SBR shows the better anti-penetration effect than EVA.

## Author contributions

YP, QZ, and GZ designed this study, YP, GZ and YQ conducted the experiments, analyzed the data and wrote the draft, QZ analyzed the data and revised the manuscript. All authors have given approval to the final version of the manuscript.

## Declaration of competing interest

The authors declare that they have no known competing financial interests or personal relationships that could have appeared to influence the work reported in this paper.

## Acknowledgements

The financial supports form Zhejiang Public Welfare Technology Application Research Project (No. LGC19E020001), The Experimental Technology Research Project of Zhejiang University (SJS202007) and National Natural Science Foundation of China (No. 51878602) are highly appreciated.

## References

[1] H. Christopher, On the history of Portland cement after 150 years, J. Chem. Educ. 53 (4) (1976) 222–223, https://doi.org/10.1021/ed053p222.
[2] J.J. Biernacki, J.W. Bullard, G. Sant, K. Brown, F.P. Glasser, S. Jones, T. Ley, R. Livingston, L. Nicoleau, J. Olek, F. Sanchez, R. Shahsavari, P.E. Stutzman, K. Sobolev, T. Prater, Cements in the 21st century: challenges, perspectives, and opportunities, J. Am. Ceram. Soc. 100 (7) (2017) 2746–2773, https://doi.org/10.1111/jace.14948.
[3] D.K. Panesar, M. Aqel, D. Rhead, H. Schell, Effect of cement type and limestone particle size on the durability of steam cured self-consolidating concrete, Cement Concr. Compos. 80 (2017) 175–189, https://doi.org/10.1016/j.cemconcomp.2017.03.007.
[4] M. Balapour, A. Joshaghani, F. Althoey, Nano-$SiO_2$ contribution to mechanical, durability, fresh and microstructural characteristics of concrete: a review, Construct. Build. Mater. 181 (2018) 27–41, https://doi.org/10.1016/j.conbuildmat.2018.05.266.
[5] T.J. Liu, S.S. Qin, D.J. Zou, W. Song, Experimental investigation on the durability performances of concrete using cathode ray tube glass as fine aggregate under chloride ion penetration or sulfate attack, Construct. Build. Mater. 163 (2018) 634–642, https://doi.org/10.1016/j.conbuildmat.2017.12.135.
[6] E. Xie, C. Zhou, Q. Song, Q. Zeng, Z. Wang, The effect of chemical aging on water permeability of white cement mortarsin the context of sol–gel science, Cement Concr. Compos. 114 (2020) 103812, https://doi.org/10.1016/j.cemconcomp.2020.103812.
[7] Q. Zeng, Z. Wang, Poroelastic insights into the stress dependence of chloride diffusivity in cement-based materials under low stresses, J. Adv. Concr. Technol. 17 (2019) 350–364, https://doi.org/10.3151/jact.17.6.350.
[8] B.J. Lee, Y.Y. Kim, Durability of latex modified concrete mixed with a shrinkage reducing agent for bridge deck pavement, Int. J. Concr. Struct. Mater. 12 (1) (2018) 23, https://doi.org/10.1186/s40069-018-0261-8.
[9] Y. Wang, M.Z. An, Z.R. Yu, S. Han, W.Y. Ji, Durability of reactive powder concrete under chloride-salt freeze–thaw cycling, Mater. Struct. 50 (1) (2017) 18, https://doi.org/10.1617/s11527-016-0878-5.
[10] P.K. Mehta, P.J.M. Monteiro, Concrete: Microstructure, Properties, and Materials, fourth ed., McGraw-Hill Education, New York, 2014. http://refhub.elsevier.com/S0008-8846(19)30188-7/rf1655.
[11] D.N. Katpady, H. Hazehara, M. Soeda, T. Kubota, S. Murakami, Durability assessment of blended concrete by air permeability, Int. J. Concr. Struct. Mater. 12 (1) (2018) 30, https://doi.org/10.1186/s40069-018-0260-9.
[12] K. Chia, M.H. Zhang, Water permeability and chloride permeability of high strength light weight aggregate concrete, Cement Concr. Res. 32 (2002) 639–645, https://doi.org/10.1016/S0008-8846(01)00738-4.
[13] S.P. Zhang, L. Zong, Evaluation of relationship between water absorption and durability of concrete materials, Ann. Mater. Sci. Eng. (2014) 1–8, https://doi.org/10.1155/2014/650373, 2014.
[14] E.J. Garboczi, Permeability, diffusivity, and microstructural parameters: a critical review, Cement Concr. Res. 20 (4) (1990) 591–601, https://doi.org/10.1016/0008-8846(90)90101-3.
[15] D.C. Hughes, Pore structure and permeability of hardened cement paste, Mag. Concr. Res. 37 (133) (1985) 227–233, https://doi.org/10.1680/macr.1985.37.133.227.
[16] X. Sun, Q. Dai, K. Ng, Computational investigation of pore permeability and connectivity from transmission X-ray microscope images of a cement paste specimen, Construct. Build. Mater. 68 (2014) 240–251, https://doi.org/10.1016/j.conbuildmat.2014.06.049.
[17] L. Li, W. Liu, Q. You, M. Chen, Q. Zeng, C. Zhou, M. Zhang, Relationships between microstructure and transport properties in mortar containing recycled ceramic powder, J. Clean. Prod. 263 (2020) 121384, https://doi.org/10.1016/j.jclepro.2020.121384.
[18] L.H. Shen, Q.H. Li, W. Ge, S.L. Xu, The mechanical property and frost resistance of roller compacted concrete by mixing silica fume and limestone powder: experimental study, Construct. Build. Mater. 239 (2020) 117882, https://doi.org/10.1016/j.conbuildmat.2019.117882.
[19] K. Behfarnia, M. Rostami, Effects of micro and nanoparticles of $SiO_2$ on the permeability of alkali activated slag concrete, Construct. Build. Mater. 131 (2017) 205–213, https://doi.org/10.1016/j.conbuildmat.2016.11.070.
[20] R. Liu, H.G. Xiao, J.L. Liu, S. Guo, Y.F. Pei, Improving the microstructure of ITZ and reducing the permeability of concrete with various water/cement ratios using nano-silica, J. Mater. Sci. 54 (1) (2018) 444–456, https://doi.org/10.1007/s10853-018-2872-5.
[21] I. Ismail, S.A. Bernal, J.L. Provis, N.R. San, D.G. Brice, A.R. Kilcullen, S. Hamdan, J. S.J. van Deventer, Influence of fly ash on the water and chloride permeability of alkali-activated slag mortars and concretes, Construct. Build. Mater. 48 (2013) 1187–1201, https://doi.org/10.1016/j.conbuildmat.2013.07.106.
[22] T. Bilir, Effects of non-ground slag and bottom ash as fine aggregate on concrete permeability properties, Construct. Build. Mater. 26 (1) (2012) 730–734, https://doi.org/10.1016/j.conbuildmat.2011.06.080.
[23] S. Tsivilis, J. Tsantilas, G. Kakali, E. Chaniotakis, A. Sakellariou, The permeability of Portland limestone cement concrete, Cement Concr. Res. 33 (9) (2003) 1465–1471, https://doi.org/10.1016/S0008-8846(03)00092-9.
[24] A. Wetzel, B. Middendorf, Influence of silica fume on properties of fresh and hardened ultra high performance concrete based on alkali-activated slag, Cement Concr. Compos. 100 (2019) 53–59, https://doi.org/10.1016/j.cemconcomp.2019.03.023.
[25] Z.M. He, A.Q. Shen, Y.C. Guo, Z.H. Lyu, D.S. Li, X. Qin, M. Zhao, Z.L. Wang, Cement-based materials modified with superabsorbent polymers: a review, Construct. Build. Mater. 225 (2019) 569–590, https://doi.org/10.1016/j.conbuildmat.2019.07.139.
[26] C.Y. Wang, Y.H. Bu, S.L. Guo, Y. Lu, B.J. Sun, Z.H. Shen, Self-healing cement composite: amine-and ammonium-based pH-sensitive superabsorbent polymers, Cement Concr. Compos. 96 (2019) 154–162, https://doi.org/10.1016/j.cemconcomp.2018.11.023.
[27] K. Rashid, M. Ahmad, M.A. Tahir, Influence of organic agents to compressive strength of cement mortar, Construct. Build. Mater. 175 (2018) 434–438, https://doi.org/10.1016/j.conbuildmat.2018.04.177.
[28] J.B. Kardon, Polymer-modified concrete: review, J. Mater. Civ. Eng. 9 (2) (1997) 85–92, https://doi.org/10.1061/(ASCE)0899-1561(1997)9:2(85).
[29] M.V. Diamanti, A. Brenna, F. Bolzoni, M. Berra, T. Pastore, M. Ormellese, Effect of polymer modified cementitious coatings on water and chloride permeability in concrete, Construct. Build. Mater. 49 (2013) 720–728, https://doi.org/10.1016/j.conbuildmat.2013.08.050.
[30] A. Pierre, A. Perrot, V. Picandet, Y. Guevel, Cellulose ethers and cement paste permeability, Cement Concr. Res. 72 (2015) 117–127, https://doi.org/10.1016/j.cemconres.2015.02.013.
[31] Z.X. Yang, X.M. Shi, A.T. Creighton, M.M. Peterson, Effect of styrene–butadiene rubber latex on the chloride permeability and microstructure of Portland cement mortar, Construct. Build. Mater. 23 (6) (2009) 2283–2290, https://doi.org/10.1016/j.conbuildmat.2008.11.011.
[32] M. Ramli, A.A. Tabassi, Effects of polymer modification on the permeability of cement mortars under different curing conditions: a correlational study that includes pore distributions, water absorption and compressive strength, Construct. Build. Mater. 28 (1) (2012) 561–570, https://doi.org/10.1016/j.conbuildmat.2011.09.004.
[33] M. Ramli, A.A. Tabassi, Influences of polymer modification and exposure conditions on chloride permeability of cement mortars and composites, J. Mater. Civ. Eng. 24 (2) (2012) 216–222, https://doi.org/10.1061/(ASCE)MT.1943-5533.0000379.

[34] N. Ukrainczyk, A. Rogina, Styrene-butadiene latex modified calcium aluminate cement mortar, Cement Concr. Compos. 41 (2013) 16–23, https://doi.org/10.1016/j.cemconcomp.2013.04.012.
[35] H.Y. Ma, Z.J. Li, Microstructures and mechanical properties of polymer modified mortars under distinct mechanisms, Construct. Build. Mater. 47 (2013) 579–587, https://doi.org/10.1016/j.conbuildmat.2013.05.048.
[36] D.A. Silva, P.J.M. Monteiro, Analysis of $C_3A$ hydration using soft X-rays transmission microscopy: effect of EVA copolymer, Cement Concr. Res. 35 (10) (2005) 2026–2032, https://doi.org/10.1016/j.cemconres.2005.02.002.
[37] D.A. Silva, P.J.M. Monteiro, The influence of polymer on the hydrationofPortland cement phases analyzed by soft X-ray transmission microscopy, Cement Concr. Res. 36 (8) (2006) 1501–1507, https://doi.org/10.1016/j.cemconres.2006.05.010.
[38] Y. Peng, Q. Zeng, S.L. Xu, G.R. Zhao, P.M. Wang, X.P. Liu, BSE-IA reveals retardation mechanisms of polymer powders on cement hydration, J. Am. Ceram. Soc. 103 (2020) 3373–3389, https://doi.org/10.1111/jace.16982.
[39] C. Wagner, B. Villmann, V. Slowik, V. Mechtcherine, Water permeability of cracked strain-hardening cement-based composites, Cement Concr. Compos. 82 (2017) 234–241, https://doi.org/10.1016/j.cemconcomp.2017.06.003.
[40] V. Picandet, D. Rangeard, A. Perrot, T. Lecompte, Permeability measurement of fresh cement paste, Cement Concr. Res. 41 (3) (2011) 330–338, https://doi.org/10.1016/j.cemconres.2010.11.019.
[41] H. Loosveldt, Z. Lafhaj, F. Skoczylas, Experimental study of gas and liquid permeability of a mortar, Cement Concr. Res. 32 (9) (2002) 1357–1363, https://doi.org/10.1016/S0008-8846(02)00793-7.
[42] A.A. Torres-Acosta, Water and chloride permeability of Cement-Based mortar with dehydrated cacti additions, J. Chem. Technol. Biotechnol. 94 (2019) 3488–3494, https://doi.org/10.1002/jctb.5938.
[43] S. Kumar, R.C. Gupta, S. Shrivastava, Strength, abrasion and permeability studies on cement concrete containing quartz sandstone coarse aggregates, Construct. Build. Mater. 125 (2016) 884–891, https://doi.org/10.1016/j.conbuildmat.2016.08.106.
[44] A. Voss, M. Pour-Ghaz, M. Vauhkonen, A. Seppänen, Electrical capacitance tomography to monitor unsaturated moisture ingress in cement-based materials, Cement Concr. Res. 89 (2016) 158–167, https://doi.org/10.1016/j.cemconres.2016.07.011.
[45] D. Smyl, Electrical tomography for characterizing transport properties in cement-based materials: a review, Construct. Build. Mater. 244 (2020) 118299, https://doi.org/10.1016/j.conbuildmat.2020.118299.
[46] J.A. Suárez-Navarro, A.M. Moreno-Reyes, C. Gascó, M.M. Alonso, F. Puertas, Gamma spectrometry and LabSOCS-calculated efficiency in the radiological characterisation of quadrangular and cubic specimens of hardened Portland cement paste, Radiat. Phys. Chem. 171 (2020) 108709, https://doi.org/10.1016/j.radphyschem.2020.108709.
[47] B.C. Öztürk, C.Ç. Kızıltepe, B. Ozden, E. Güler, S. Aydın, Gamma and neutron attenuation properties of alkali-activated cement mortars, Radiat. Phys. Chem. 166 (2020) 108478, https://doi.org/10.1016/j.radphyschem.2019.108478.
[48] P. Zhang, P.G. Wang, D.S. Hou, Z.L. Liu, M. Haist, T.J. Zhao, Application of neutron radiography in observing and quantifying the time-dependent moisture distributions in multi-cracked cement-based composites, Cement Concr. Compos. 78 (2017) 13–20, https://doi.org/10.1016/j.cemconcomp.2016.12.006.
[49] P. Zhang, F.H. Wittmann, P. Lura, H.S. Müller, S.B. Han, T.J. Zhao, Application of neutron imaging to investigate fundamental aspects of durability of cement-based materials: a review, Cement Concr. Res. 108 (2018) 152–166, https://doi.org/10.1016/j.cemconres.2018.03.003.
[50] A. Bogner, J. Link, M. Baum, M. Mahlbacher, T. Gil-Diaz, J. Lützenkirchen, T. Sowoidnich, F. Heberling, T. Schäfer, H.M. Ludwig, F. Dehn, H.S. Müller, M. Haist, Early hydration and microstructure formation of Portland cement paste studied by oscillation rheology, isothermal calorimetry, 1H NMR relaxometry, conductance and SAXS, Cement Concr. Res. 130 (2020) 105977, https://doi.org/10.1016/j.cemconres.2020.105977.
[51] M.A. Javed, S. Komulainen, H. Daigle, B.Y. Zhang, J. Vaara, B. Zhou, V.V. Telkki, Determination of pore structures and dynamics of fluids in hydrated cements and natural shales by various 1H and 129Xe NMR methods, Microporous Mesoporous Mater. 281 (2019) 66–74, https://doi.org/10.1016/j.micromeso.2019.02.034.
[52] S.X. Hong, W.Q. Yao, B.W. Guo, C. Lin, B.Q. Dong, W.W. Li, D.S. Hou, F. Xing, Water distribution characteristics in cement paste with capillary absorption, Construct. Build. Mater. 240 (2020) 117767, https://doi.org/10.1016/j.conbuildmat.2019.117767.
[53] S. X Hong, S.F. Qin, W.Q. Yao, B.W. Guo, D.S. Hou, Y.X. Zhang, W. Liu, W.W. Li, B. Q. Dong, Visualized tracing of capillary absorption process in cementitious material based on X ray computed tomography, Cement Concr. Compos. 107 (2020) 103487, https://doi.org/10.1016/j.cemconcomp.2019.103487.
[54] J.Z. Liu, M.F. Ba, Y.G. Du, Z.M. He, J.B. Chen, Effects of chloride ions on carbonation rate of hardened cement paste by X-ray CT techniques, Construct. Build. Mater. 122 (2016) 619–627, https://doi.org/10.1016/j.conbuildmat.2016.06.101.
[55] Y.C. Wang, Z.Y. Li, S.H. Wang, W.G. Yang, W. Liu, L.Y. Li, L.P. Tang, F. Xing, Analysis methodology of XCT results for testing ingress of substances in hardened cement paste: explained with chloride immersion test, Construct. Build. Mater. 229 (2019) 116839, https://doi.org/10.1016/j.conbuildmat.2019.116839.
[56] J.D. Han, W. Sun, G.H. Pan, C.H. Wang, Monitoring the evolution of accelerated carbonation of hardened cement pastes by X-ray computed tomography, J. Mater. Civ. Eng. 25 (3) (2013) 347–354, https://doi.org/10.1061/(ASCE)MT.1943-5533.0000610.
[57] W.J. Long, Y. Gu, B.X. Xiao, Q. Zhang, F. Xing, Micro-mechanical properties and multi-scaled pore structure of graphene oxide cement paste: synergistic application of nanoindentation, X-ray computed tomography, and SEM-EDS analysis, Construct. Build. Mater. 179 (2018) 661–674, https://doi.org/10.1016/j.conbuildmat.2018.05.229.
[58] H.Z. Zhang, B. Šavija, M. Luković, E. Schlangen, Experimentally informed micromechanical modelling of cement paste: an approach coupling X-ray computed tomography and statistical nanoindentation, Composites Part B 157 (2019) 109–122, https://doi.org/10.1016/j.compositesb.2018.08.102.
[59] Z. Ranachowski, D. Jóźwiak-Niedźwiedzka, P. Ranachowski, M. Dąbrowski, S. Kúdela Jr., T. Dvorak, The determination of diffusive tortuosity in concrete specimens using X-ray microtomography, Arch. Metall. Mater. 60 (2) (2015) 1115–1119, https://doi.org/10.1515/amm-2015-0140.
[60] M.A.B. Promentilla, T. Sugiyama, T. Hitomi, N. Takeda, Quantification of tortuosity in hardened cement pastes using synchrotron-based X-ray computed microtomography, Cement Concr. Res. 39 (6) (2009) 548–557, https://doi.org/10.1016/j.cemconres.2009.03.005.
[61] A. Akhavan, S. Shafaatian, F. Rajabipour, Quantifying the effects of crack width, tortuosity, and roughness on water permeability of cracked mortars, Cement Concr. Res. 42 (2) (2012) 313–320, https://doi.org/10.1016/j.cemconres.2011.10.002.
[62] Y. Su, N. Hossiney, M. Tia, The analysis of air voids in concrete specimen using X-ray computed tomography, Proc. SPIE (2013) 8694, https://doi.org/10.1117/12.2012267, 86940S.
[63] T. Oesch, F. Weise, D. Meinel, C. Gollwitzer, Quantitative in-situ analysis of water transport in concrete completed using X-ray computed tomography, Transport Porous Media 127 (2) (2018) 371–389, https://doi.org/10.1007/s11242-018-01228-0.
[64] L. Yang, Y.S. Zhang, Z.Y. Liu, P. Zhao, C. Liu, In-situ tracking of water transport in cement paste using X-ray computed tomography combined with CsCl enhancing, Mater. Lett. 160 (2015) 381–383, https://doi.org/10.1016/j.matlet.2015.08.011.
[65] C. Hall, W.D. Hoff, Water Transport in Brick, Stone and Concrete, second ed., CRC Press, 2011 https://doi.org/10.1201/b12840.
[66] C.S. Willson, N. Lu, W.J. Likos, Quantification of grain, pore, and fluid microstructure of unsaturated sand from X-ray computed tomography images, Geotech. Test J. 35 (6) (2012) 911–923, https://doi.org/10.1520/GTJ20120075.
[67] S. Brisard, M. Serdar, P.J. M Monteiro, Multiscale X-ray tomography of cementitious materials: a review, Cement Concr. Res. 128 (2020) 105824, https://doi.org/10.1016/j.cemconres.2019.105824.
[68] J.J. Hubell, S.M. Seltzer, Tables of X-Ray Mass Attenuation Coefficients and Mass Energy-Absorption Coefficients 1 keV to 20 MeV for Elements Z= 1 to 92 and 48 Additional Substances of Dosimetric Interest, NIST-PL, Ionizing Radiation Div, Gaithersburg, MD, USA, 1995. https://physics.nist.gov/PhysRefData/XrayMassCoef/tab3.html.
[69] K.O. Kjellsen, A. Monsøy, K. Isachsen, R.J. Detwiler, Preparation of flat-polished specimens for SEM-backscattered electron imaging and X-ray microanalysis-importance of epoxy impregnation, Cement Concr. Res. 33 (4) (2003) 611–616, https://doi.org/10.1016/S0008-8846(02)01029-3.
[70] K. Wu, H.S. Shi, L.L. Xu, G. Ye, G. De Schutter, Microstructural characterization of ITZ in blended cement concretes and its relation to transport properties, Cement Concr. Res. 79 (2016) 243–256, https://doi.org/10.1016/j.cemconres.2015.09.018.
[71] C. Shi, X. Zou, L. Yang, P. Wang, M. Niu, Influence of humidity on the mechanical properties of polymer-modified cement-based repair materials, Construct. Build. Mater. 261 (2020), https://doi.org/10.1016/j.conbuildmat.2020.119928, 119928.
[72] N. Matubayasi, K. Yamamoto, S.I. Yamaguchi, H. Matsuo, N. Ikeda, Thermodynamic quantities of surface formation of aqueous electrolyte solutions: III. Aqueous solutions of alkali metal chloride, J. Colloid Interface Sci. 214 (1) (1999) 101–105, https://doi.org/10.1006/jcis.1999.6172.
[73] T. Nakai, S. Sawamura, Y. Taniguchi, Y. Yamaura, Effect of pressure on the viscosity B coefficient of cesium chloride in water, J. Soc. Mater. Sci., Jpn. 45 (9) (1996) 143–147, https://doi.org/10.2472/jsms.45.9Appendix_143.
[74] P. Wang, Q. Zhang, M. Wang, B. Yin, D. Hou, Y. Zhang, Atomistic insights into cesium chloride solution transport through the ultra-confined calcium-silicate-hydrate channel, Phys. Chem. Chem. Phys. 21 (22) (2019) 11892–11902, https://doi.org/10.1039/C8CP07676F.
[75] L. Li, R. Wang, S.K. Zhang, Effect of curing temperature and relative humidity on the hydrates and porosity of calcium sulfoaluminate cement, Construct. Build. Mater. 213 (2019) 627–636, https://doi.org/10.1016/j.conbuildmat.2019.04.044.
[76] F.K. Saleh, C. Teodoriu, C.H. Sondergeld, Investigation of the effect of cement mixing energy on cement strength and porosity using NMR and UPV methods, J. Nat. Gas Sci. Eng. 70 (Oct. 2019) 102972, https://doi.org/10.1016/j.jngse.2019.102972.
[77] C. Zhang, X. Kong, Z. Lu, D. Jansen, J. Pakusch, S. Wang, Pore structure of hardened cement paste containing colloidal polymers withvaried glass transition temperature and surface charges, Cement Concr. Compos. 95 (2019) 154–168, https://doi.org/10.1016/j.cemconcomp.2018.11.001.
[78] J.F. Ma, Y.Z. Shang, C.J. Peng, H.L. Liu, S.Z. Zheng, H.X. Zhao, S. Qi, Q.P. Ran, Synthesis, characterization, and performance of novelphosphate-modified polymers as air-entraining agents, Construct. Build. Mater. 232 (2020) 117231, https://doi.org/10.1016/j.conbuildmat.2019.117231.
[79] S. Riyazi, J.T. Kevern, M. Mulheron, Super absorbent polymers (SAPs) as physical air entrainment in cement mortars, Construct. Build. Mater. 147 (2017) 669–676, https://doi.org/10.1016/j.conbuildmat.2017.05.001.
[80] K. Wu, J.F. Long, L.L. Xu, G. De Schutter, A study on the chloride diffusion behavior of blended cement concrete in relation to aggregate and ITZ, Construct. Build. Mater. 223 (2019) 1063–1073, https://doi.org/10.1016/j.conbuildmat.2019.07.068.

[81] Q. Zeng, Z. Lin, C.S. Zhou, J.Y. Wang, Capillary imbibition of ethanol in cement paste traced by X-ray computed tomography with CsCl-enhancing technique, Chem. Phys. Lett. 726 (Jul) (2019) 117–123, https://doi.org/10.1016/j.cplett.2019.04.022.

[82] C.L. Hu, Z.J. Li, A review on the mechanical properties of cement-based materials measured by nanoindentation, Construct. Build. Mater. 90 (Aug. 2015) 80–90, https://doi.org/10.1016/j.conbuildmat.2015.05.008.

[83] K. Wu, H. Han, L.L. Xu, X.J. Yang, G. De Schutter, Supported ITZ modification efficiencies via surface coating nanoparticles on aggregate and its influence on properties, Materials 12 (21) (2019) 3541, https://doi.org/10.3390/ma122135413541.

[84] H.S. Wong, M. Zobel, N.R. Buenfeld, R.W. Zimmerman, Influence of the interfacial transition zone and microcracking on the diffusivity, permeability and sorptivity of cement-based materials after drying, Mag. Concr. Res. 61 (8) (2009) 571–589, https://doi.org/10.1680/macr.2008.61.8.571.

[85] A.G. Cid, R. Rosenkranz, M. Loffler, A. Clausner, Y. Standke, E. Zschech, Quantitative analysis of backscattered electron (BSE) contrast using low voltage scanning electron microscopy (LVSEM) and its application to $Al_{0.22}Ga_{0.78}N$/GaN layers, Ultramicroscopy 195 (2018) 47–52, https://doi.org/10.1016/j.ultramic.2018.08.026.

[86] N.D.M. Evans, Binding mechanisms of radionuclides to cement, Cement Concr. Res. 38 (4) (2008) 543–553, https://doi.org/10.1016/j.cemconres.2007.11.004.

[87] R. O Abdel Rahman, D.H.A. Zin El Abidin, H. Abou-Shady, Cesium binding and leaching from single and binary contaminant cement–bentonite matrices, Chem. Eng. J. 245 (2014) 276–287, https://doi.org/10.1016/j.cej.2014.02.033.

[88] R. Druteikienė, J. Šapolaitė, Ž. Ežerinskis, L. Juodis, Batch-type study of Cs, Co, and Tc binding with hydrated cement under hyperalkaline conditions, J. Radioanal. Nucl. Chem. 313 (2) (2017) 299–307, https://doi.org/10.1007/s10967-017-5303-1.

[89] J. Arayro, A. Dufresne, T. Zhou, K. Ioannidou, J.F. Ulm, R. Pellenq, L.K. Béland, Thermodynamics, kinetics, and mechanics of cesium sorption in cement paste: a multiscale assessment, Phys. Rev. Mater. 2 (5) (2018), 053608, https://doi.org/10.1103/PhysRevMaterials.2.053608.

[90] E. Knapen, D. Van Gemert, Cement hydration and microstructure formation in the presence of water-soluble polymers, Cement Concr. Res. 39 (1) (2009) 6–13, https://doi.org/10.1016/j.cemconres.2008.10.003.